

# Spin-3/2 physics of semiconductor hole nanowires: Valence-band mixing and tunable interplay between bulk-material and orbital bound-state spin splittings

D. Csontos,<sup>1</sup> P. Brusheim,<sup>2,3</sup> U. Zülicke,<sup>1,4</sup> and H. Q. Xu<sup>2</sup>

<sup>1</sup>*Institute of Fundamental Sciences and MacDiarmid Institute for Advanced Materials and Nanotechnology, Massey University (Manawatu Campus), Private Bag 11 222, Palmerston North, New Zealand*

<sup>2</sup>*Division of Solid State Physics, Lund University, Box 118, S-22100 Lund, Sweden*

<sup>3</sup>*Institute of High Performance Computing, 1 Fusionopolis Way, #16-16 Connexis, Singapore 138632, Singapore*

<sup>4</sup>*Centre for Theoretical Chemistry and Physics, Massey University (Albany Campus), Private Bag 102904, North Shore MSC, Auckland 0745, New Zealand*

(Dated: March 4, 2022)

We present a detailed theoretical study of the electronic spectrum and Zeeman splitting in hole quantum wires. The spin-3/2 character of the topmost bulk-valence-band states results in a strong variation of subband-edge  $g$  factors between different subbands. We elucidate the interplay between quantum confinement and heavy-hole – light-hole mixing and identify a certain robustness displayed by low-lying hole-wire subband edges with respect to changes in the shape or strength of the wire potential. The ability to address individual subband edges in, e.g., transport or optical experiments enables the study of holes states with nonstandard spin polarization, which do not exist in spin-1/2 systems. Changing the aspect ratio of hole wires with rectangular cross-section turns out to strongly affect the  $g$  factor of subband edges, providing an opportunity for versatile in-situ tuning of hole-spin properties with possible application in spintronics. The relative importance of cubic crystal symmetry is discussed, as well as the spin splitting away from zone-center subband edges.

## I. INTRODUCTION

Self-assembled semiconductor nanowires have attracted a lot of attention recently due to their well-defined crystalline structure, unique electrical and optical properties, as well as a promising outlook for their use as building blocks in nanoelectronics, nanospintronics and nanobiotechnology.<sup>1–32</sup> Rapid developments in material science and technology have enabled the realization of nanowires from many materials and materials combinations, such as III-V semiconductors (e.g., GaAs,<sup>1,22,27</sup> InP,<sup>2,3,10,12</sup> InAs<sup>1,7,8,29</sup>), II-VI semiconductors (e.g., CdSe,<sup>5,12</sup> CdS,<sup>12</sup> CdTe,<sup>4,25</sup> ZnTe<sup>20,32</sup>), as well as Si<sup>14,24,28</sup> and Ge.<sup>23,30,31</sup> By now it is possible to dope nanowires<sup>22,26,29</sup> and perform heterostructure engineering with atomic precision.<sup>7,8,12,17</sup> This enabled the realization of  $p$ -type<sup>22,26</sup> or ambipolar<sup>29</sup> transport characteristics, as well as the fabrication of nanostructures (quantum dots,<sup>8</sup> rods,<sup>20</sup> and superlattices<sup>9</sup>). Based on these material-science developments, devices such as nanowire diodes,<sup>1,3</sup> superlattices for nanoscale photonics and electronics,<sup>9</sup> lasers,<sup>6,16</sup> resonant tunneling diodes,<sup>8</sup> and light-emitting diodes,<sup>1,3,12</sup> have been demonstrated.

Another area of significant research that has emerged in recent years focuses on the study of the spin degree of freedom. This is relevant for the fundamental understanding of spin phenomena in solid-state systems, but also for potential applications that utilize the spin, rather than the charge degree of freedom, in electronics.<sup>33,34</sup> Spin injection, manipulation and detection has been achieved with the use of magnetic fields and diluted magnetic semiconductors.<sup>35,36</sup> A complementary direction of current spin-electronics research is based on the quantum-mechanical coupling between spin and orbital degrees of freedom. For example, the tunability of structural inversion-asymmetry induced spin-orbit (SO) coupling<sup>37</sup> could be used to manipulate spin-polarized currents in ballistic mesoscopic channels.<sup>38</sup>

To study SO effects in semiconductors, charge carriers from the valence band (i.e., holes) are particularly interesting since they are subject to an inherently strong SO coupling even in the bulk. In addition, as valence-band states are predominantly  $p$ -like (i.e., have orbital angular momentum  $L = 1$ ), they are characterized by a total angular momentum of either  $J = 3/2$  or  $J = 1/2$ . The topmost valence bands are described by the former; thus they behave like spin-3/2 particles and, when confined in nanostructures, exhibit quite counter-intuitive quantum effects. For example, the spin-3/2 nature of the topmost valence bands leads to large anisotropies of the hole  $g$  factor in quantum wells,<sup>39,40</sup> wires,<sup>27</sup> point contacts,<sup>41,42</sup> quantum dots,<sup>43–45</sup> and localized acceptor states.<sup>46</sup>

The bulk dispersions for the conduction and valence bands of a typical semiconductor in zero magnetic field are shown

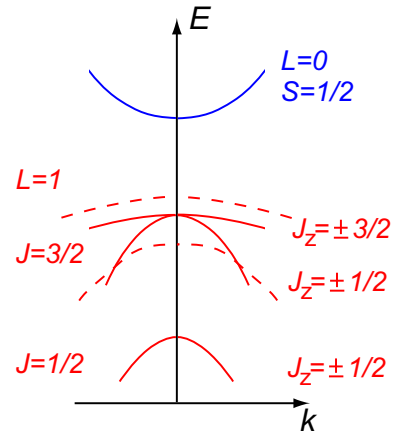


FIG. 1: (Color online) Schematic dispersion of bulk-semiconductor conduction and valence bands (solid lines). The dashed lines depict a situation where the  $J = 3/2$  valence bands are split due to quantum confinement, e.g., in a two-dimensional hole gas.

as the solid curves in Fig. 1. The four-fold degeneracy of the  $J = 3/2$  valence-band edges is lifted at finite wave vector  $\mathbf{k}$ ,<sup>47</sup> giving rise to separated heavy-hole (HH) and light-hole (LH) branches whose states are distinguished by the  $z$ -axis spin-3/2 projection quantum numbers  $J_z = \pm 3/2$  and  $J_z = \pm 1/2$ , respectively. Size quantization, e.g., due to a quantum-well confinement, causes an energy splitting between the quasi-twodimensional (2D) HH and 2D LH band edges.<sup>39,48,49</sup> This HH-LH *splitting* is illustrated by the dashed lines in Fig. 1. At finite wave vector  $\mathbf{k}_\perp$  for motion perpendicular to the quantum-well growth direction, a HH-LH *mixing* occurs that can give rise to level anticrossings,<sup>39</sup> further increasing the complexity of holes' electronic properties.

While in 2D systems the HH-LH mixing is absent at the subband edge and can be assumed to have a small magnitude for finite  $k_\perp$  in the presence of strong quantum confinement,<sup>50</sup> this is not the case for hole nanowires<sup>27,51–55</sup> and quantum dots.<sup>56–59</sup> Previous studies of the topmost hole-nanowire eigenstates have shown that they are, to a varying degree, mixtures of HH and LH states.<sup>55,60</sup> This has been found to influence, e.g., the spin splitting in cylindrical hole nanowires with hard-wall confinement<sup>55,60,61</sup> and nanosized clusters.<sup>62</sup>

In this article, we present an extensive theoretical study of the electronic structure of hole nanowires, focusing especially on the importance of HH-LH mixing and splitting. Furthermore, we have investigated the ramifications of the spin-3/2 nature of holes for the spin splitting of hole nanowire states, in particular elucidating the interplay between the bulk-material and bound-state orbital effects due to a magnetic field.

We use the Luttinger description<sup>47</sup> of the semiconductor valence band to study the subband edges ( $k_z = 0$ ) of hole nanowires oriented along the  $z$  direction. In order to quantitatively analyze the strength of HH-LH mixing at the subband edge states, we make use of scalar invariants obtainable from a decomposition of the spin-3/2 density matrix in terms of a multipole expansion.<sup>63</sup> The squared dipole moment, which apart from a prefactor is a measure of the squared magnitude of the hole-spin polarization, is by its definition<sup>63</sup> independent of the quantization axis of the angular momentum used in the basis functions of the hole subband edge state. Thus, it provides a rigorous, basis-independent way of characterizing the hole-spin polarization character of hole subband edge states.

We present a comprehensive analysis of the hole-spin polarization character of hole subband edge states in nanowires with different confining potentials. The strong HH-LH mixing manifests as large spatial variations in the hole-spin polarization density profile of individual subband states. Furthermore, we observe large differences between the hole-spin polarization density profiles of different subband states. We also find that the topmost hole subband edges in general display universal features that are robust against changes of the confining potential's symmetry. For hole subband edge states that are far away from the bulk valence band edge, however, differences in the strength and shape of the confining potential significantly affect the wavefunction's hole-spin polarization.

A direct manifestation of the strong HH-LH mixing (and splitting) in hole nanowires is observed in the spin splitting due to a finite magnetic field. We use perturbative and nu-

merical calculations to show that, in a magnetic field applied parallel to the wire axis, the effective  $g$  factor varies strongly between different wire subband edges. We analyze the separate contributions to the  $g$  factor arising from bulk-material and orbital bound-state interactions with the magnetic field. We find that the hole envelope functions acquire large orbital momentum due to the imposed quantum confinement, which strongly affects the effective  $g$  factor of hole nanowire states. Interestingly, the bulk-material and bound-state contributions can come with the same or opposite sign, thus effectively enhancing or suppressing each other's contribution to the total spin splitting. We also find that the interplay between the two contributions is very sensitive to the hole wave function, and thus, that the  $g$  factor of individual wire states can be tuned by changing the confining potential. For example, we show that by changing the aspect ratio of the lateral dimensions of a wire with rectangular crosssection, one can tune the magnitude and even the sign of the  $g$  factor quite sensitively. Such a situation can, in principle, be easily realized by tuning the lateral confinement via side gates in self-assembled<sup>64,65</sup> or lithographically defined nanowires,<sup>66</sup> or quantum point contacts.<sup>67–69</sup> Quasi-one-dimensional (1D) hole systems thus provide an interesting laboratory for the study of spin-3/2 physics, as well as have the potential for being building blocks in hole-spintronics applications.

In the following, we start by presenting the basic theoretical formalism for describing hole-nanowire states in the absence of a magnetic field within the Luttinger model (Sec. II). Subsequently, we will discuss the influence of valence-band mixing on hole-nanowire subband edges ( $k_z = 0$ ) in Sec. III, using scalar invariants from the decomposition of the spin-3/2 density matrix to provide a comprehensive analysis of the hole-spin polarization of nanowire subband edges. A discussion of the influence of symmetry and strength of the confining potential will be given. Next, the spin splitting of hole-nanowire subband edges due to an applied magnetic field is discussed in Sec. IV. We provide the theoretical description of bulk-material and bound-state orbital interactions with a magnetic field in Sec. IV A, followed by a detailed analysis of their individual contribution to the total  $g$  factor of hole-nanowire states in Secs. IV B and IV C. The effects of lower-symmetry corrections and finite  $k_z$  will be considered in Secs. IV D and IV F. We discuss the important interplay between bulk-material and orbital contributions to the total  $g$  factors of hole nanowire states in Sec. IV E, demonstrating a versatile tunability of the magnitude and sign of the  $g$  factor by simple confinement engineering. We provide a summary and conclusions in Sec. V.

## II. THEORETICAL DESCRIPTION OF HOLE NANOWIRE SUBBANDS IN THE ABSENCE OF A MAGNETIC FIELD

### A. Luttinger model for bulk semiconductor valence bands

The electronic structure of bulk valence bands can be described using the Luttinger Hamiltonian<sup>47</sup>

$$H_L = -\frac{\hbar^2}{2m_0} [(\gamma_1 + 5\gamma_2/2)\hat{k}^2 - 2\gamma_2(\hat{k}_x^2 \hat{J}_x^2 + \text{cp}) - 4\gamma_3(\{\hat{k}_x, \hat{k}_y\}\{\hat{J}_x, \hat{J}_y\} + \text{cp})] , \quad (1)$$

where  $m_0$  is the vacuum electron mass,  $\hat{k}_i$  are the components of linear orbital momentum,  $\hat{J}_i$  are the Cartesian angular-momentum operators for a particle with spin  $\frac{3}{2}$ , and  $\gamma_i$  the Luttinger parameters. In Eq. (1), we have used the notation  $\{A, B\} = \frac{1}{2}(AB + BA)$ . We will choose our quantization axis for total (spin-3/2) angular momentum to be along the  $z$ -direction. In this representation,  $\hat{J}_z$  will be diagonal with eigenvalues  $\pm\frac{3}{2}$  and  $\pm\frac{1}{2}$ . The majority of the results presented in this paper focus on the properties of subband edge properties at  $k_z = 0$  and, hence, we restrict our discussion of the theoretical formalism to this case in the following unless otherwise indicated. At the end of the paper, we will discuss

hole-nanowire dispersions as a function of  $k_z$ , as well as address the issue<sup>52,53</sup> of subband edges occurring at finite  $k_z$ .

To provide clearer interpretations of our results, we will initially use the Luttinger Hamiltonian in the spherical approximation<sup>70</sup> where band warping terms due to cubic-symmetry corrections<sup>71</sup> are neglected. Formally, the spherical approximation consists of setting  $\gamma_2 \rightarrow \gamma_s$  and  $\gamma_3 \rightarrow \gamma_s$  with  $\gamma_s = (2\gamma_2 + 3\gamma_3)/5$ . At the end of the paper, we will explicitly discuss the effects of cubic corrections. In the spherical approximation (and for  $k_z = 0$ ), the bulk Hamiltonian (1) simplifies to

$$H_L^s = -\frac{\hbar^2}{2m_0} [\gamma_1 \hat{k}_\perp^2 \cdot \mathbb{1}_{4 \times 4} + \gamma_s \hat{k}_\perp^2 (\hat{J}_z^2 - \frac{5}{4} \cdot \mathbb{1}_{4 \times 4}) - \gamma_s (\hat{k}_-^2 \hat{J}_+^2 + \hat{k}_+^2 \hat{J}_-^2)] , \quad (2)$$

where  $\hat{k}_\pm = \hat{k}_x \pm i\hat{k}_y$ ,  $\hat{k}_\perp^2 = \hat{k}_x^2 + \hat{k}_y^2$ , and  $\hat{J}_\pm = (\hat{J}_x \pm i\hat{J}_y) / \sqrt{2}$ . The parameter  $\gamma_s$  is a measure of the strength of the SO coupling that is responsible for lifting the four-fold degeneracy for  $k \neq 0$ . This arises through the second term in Eq. (2), which describes the *energy splitting* between HH and LH bands. The third term is responsible for HH-LH *mixing* through the operators  $\hat{J}_\pm$ , which couple HH and LH amplitudes of the hole wave function. Thus, for  $k_\perp \neq 0$  and finite  $\gamma_s$ , the bulk valence bands can no longer be identified as being of purely HH or LH character in the sense of having definite spin projections  $J_z = \pm\frac{3}{2}$  or  $J_z = \pm\frac{1}{2}$ .<sup>55</sup> In the following discussions, we will restrict the use of the HH and LH labels solely for states that are pure HH or LH states in this sense. In the presence of a two-dimensional confining potential, such as in a quantum wire along the  $z$  direction, even states at the band edges have a finite  $k_\perp$  due to quantum confinement and thus are HH-LH mixtures.<sup>51,55</sup>

## B. Description of hole states in nanowires

We will now provide a theoretical description for subbands in hole nanowires confined by potentials with different strengths and confining potentials. We will start off by studying cylindrical hole nanowires confined by an infinite, hard-wall potential of radius  $R$ , which is particularly interesting due to its symmetry. We note that such wires can be readily fabricated by self-assembly.<sup>18</sup>

In the spherical approximation, the sum of the angular momenta  $\hat{\mathbf{J}}$  of the band-edge Bloch functions and  $\hat{\mathbf{L}}$  of the enve-

lope functions is a constant of the motion.<sup>70,71</sup> This conserved operator  $\hat{\mathbf{F}} = \hat{\mathbf{J}} + \hat{\mathbf{L}}$ , which is similar to a total angular momentum, was first used by Baldereschi and Lipari<sup>70,71</sup> to simplify the acceptor-state problem utilizing an analogy between  $\hat{\mathbf{L}}$  and  $\hat{\mathbf{J}}$  and the  $L$ - $S$  coupling scheme in atomic physics. Sercel and Vahala<sup>72,73</sup> extended this approach to study spherical quantum dots and cylindrical wires. Their formalism will be the starting point for our own investigations of the properties of hole nanowires.

We take the quantum-wire axis to be parallel to the spin-3/2 quantization axis (i.e., the  $z$  direction). The wire Hamiltonian  $H_L^s + V_{\text{ch}}(r)$  [including the cylindrical hard-wall potential:  $V_{\text{ch}}(r) = 0$  for  $r < R$  and  $V_{\text{ch}}(r) = \infty$  elsewhere] has common eigenstates with  $\hat{F}_z = \hat{J}_z + \hat{L}_z$ . Furthermore, it is a property of the Luttinger Hamiltonian that, at  $k_z = 0$ , each block labeled by a fixed quantum number  $F_z$  further decouples into two  $2 \times 2$  blocks according to

$$(H_L^s)_{F_z} = \begin{bmatrix} H_{F_z}^+ & 0 \\ 0 & H_{F_z}^- \end{bmatrix} , \quad (3)$$

where the  $H_{F_z}^\sigma$  are  $2 \times 2$  matrices acting in the Hilbert subspaces spanned by states with spin projections  $J_z = (\frac{3}{2}, -\frac{1}{2})$  (for  $\sigma = +$ ) and  $J_z = (\frac{1}{2}, -\frac{3}{2})$  (for  $\sigma = -$ ), respectively.<sup>73</sup>

To determine bulk-hole states at zero magnetic field ( $B_z = 0$ ) that can be used to construct cylindrical-wire subband states, we use polar coordinates  $(r, \phi)$  and the wave function

ansatz<sup>55,73</sup>

$$\psi(r, \phi) = e^{iF_z \phi} \begin{pmatrix} a_{F_z}^{(\text{ch})} J_{F_z-3/2}(k_{\perp} r) e^{-3i\phi/2} \\ b_{F_z}^{(\text{ch})} J_{F_z+1/2}(k_{\perp} r) e^{i\phi/2} \\ c_{F_z}^{(\text{ch})} J_{F_z-1/2}(k_{\perp} r) e^{-i\phi/2} \\ d_{F_z}^{(\text{ch})} J_{F_z+3/2}(k_{\perp} r) e^{3i\phi/2} \end{pmatrix}, \quad (4)$$

where  $J_n(k_{\perp} r)$  is an integer Bessel function and  $a_{F_z}^{(\text{ch})} \dots d_{F_z}^{(\text{ch})}$  are constants. Diagonalization of  $(H_L^s)_{F_z}$  in this representation yields the following bulk-hole eigenstates

$$\psi_{+F_z\nu}(r, \phi) = e^{iF_z \phi} \begin{pmatrix} a_{\nu}^{(\text{ch})} J_{F_z-3/2}(k_{\perp}^{\nu} r) e^{-3i\phi/2} \\ b_{\nu}^{(\text{ch})} J_{F_z+1/2}(k_{\perp}^{\nu} r) e^{i\phi/2} \\ 0 \\ 0 \end{pmatrix}, \quad (5)$$

and

$$\psi_{-F_z\nu}(r, \phi) = e^{iF_z \phi} \begin{pmatrix} 0 \\ 0 \\ b_{\nu}^{(\text{ch})} J_{F_z-1/2}(k_{\perp}^{\nu} r) e^{-i\phi/2} \\ a_{\nu}^{(\text{ch})} J_{F_z+3/2}(k_{\perp}^{\nu} r) e^{3i\phi/2} \end{pmatrix}. \quad (6)$$

In Eqs. (5) and (6) the subscript index  $\nu = \pm$  labels eigenstates *within* the  $2 \times 2$  subspaces spanned by HH and LH states with spin projections  $J_z = \pm \frac{3}{2}$  and  $J_z = \mp \frac{1}{2}$ , respectively. We emphasize that, for  $k_{\perp} \neq 0$ , hole bands are no longer of a purely HH or LH type, hence we use the generic label  $\nu = \pm$ .

The coefficients  $a_{\nu}^{(\text{ch})}, b_{\nu}^{(\text{ch})}$ , which do not depend on  $F_z$  (nor on  $\sigma$  at  $B_z = 0$ ), are given by<sup>73</sup>

$$a_{\nu}^{(\text{ch})} = -\frac{1}{\sqrt{3}}; \quad b_{\nu}^{(\text{ch})} = \sqrt{3}. \quad (7)$$

The corresponding eigenenergies are

$$E_{\nu}(k_{\perp}) = -\frac{\hbar^2 k_{\perp}^2}{2m_0} (\gamma_1 - 2\nu\gamma_s). \quad (8)$$

A generalization of these results for finite  $z$  component of the magnetic field was presented in Ref. 55. There it was pointed out that an interesting crossover occurs with increasing  $k_{\perp}$  for the effective  $g$  factor of bulk hole valence bands in the presence of a finite  $B_z$  (see Fig. 2 of Ref. 55). For  $k_{\perp} = 0$ , the spin splitting of the bulk-hole bands is characterized (in absolute terms) by the  $g$  factors  $g = 6\kappa$  and  $g = 2\kappa$ , which follows from the form of the bulk-hole Zeeman Hamiltonian that will be introduced in Eq. (15). However, at large  $k_{\perp}$ , spin splitting turns out to be characterized by  $g = 0$  and  $g = 4\kappa$ . This situation is reminiscent of the Zeeman effect in two-dimensional hole systems subject to an in-plane magnetic field,<sup>39</sup> a result that will also be significant for our later discussion of the spin splitting of a particular class of cylindrical hole-nanowire subband edges.

Quantum wire eigenstates with subband index  $\alpha$  are formed by superimposing bulk-hole eigenstates according to

$$\Psi_{\sigma F_z}^{(\alpha, \text{ch})}(r, \phi) = c_{\sigma F_z+}^{\alpha} \psi_{\sigma F_z+} + c_{\sigma F_z-}^{\alpha} \psi_{\sigma F_z-}. \quad (9)$$

The subband eigenenergies  $E_{\sigma F_z}^{(\alpha, \text{ch})}$  and expansion coefficients  $c_{\sigma F_z\nu}^{\alpha}$  are obtained by imposing the hard-wall boundary condition  $\Psi_{\sigma F_z}^{(\alpha, \text{ch})}(R, \phi) = 0$  and solving the secular equations

$$a_{+}^{(\text{ch})} b_{-}^{(\text{ch})} J_{F_z-3/2}(k_{\perp}^{+} R) J_{F_z+1/2}(k_{\perp}^{-} R) - a_{-}^{(\text{ch})} b_{+}^{(\text{ch})} J_{F_z-3/2}(k_{\perp}^{-} R) J_{F_z+1/2}(k_{\perp}^{+} R) = 0 \quad (10)$$

$$b_{+}^{(\text{ch})} a_{-}^{(\text{ch})} J_{F_z-1/2}(k_{\perp}^{+} R) J_{F_z+3/2}(k_{\perp}^{-} R) - b_{-}^{(\text{ch})} a_{+}^{(\text{ch})} J_{F_z-1/2}(k_{\perp}^{-} R) J_{F_z+3/2}(k_{\perp}^{+} R) = 0. \quad (11)$$

Again, a generalization for the case of finite magnetic field was presented earlier in Ref. 55. Hole nanowire subband edges can thus be obtained in a semi-analytical fashion for a cylindrical hard-wall confining potential.

We have also investigated hole nanowires defined by confining potentials with other symmetry and strength, in order to gauge the universality of our findings. In particular, we have focused on two additional cases, hard-wall confined hole wires with *square* (and rectangular) crosssection, and cylindrical hole nanowires confined by a *harmonic* potential.

The first case corresponds to a confining potential that is given by

$$V_{\text{rh}}(x, y) = 0 \quad \text{for } 0 \leq x < W_x \text{ and } 0 \leq y < W_y \\ V_{\text{rh}}(x, y) = \infty \quad \text{elsewhere},$$

where  $W_{x,y}$  are the lateral wire dimensions and  $W_x = A \cdot W_y$ . We will first consider a square-crosssection case with  $A = 1$ , deferring a discussion of the dependence on aspect ratio  $A$  to the end of our paper. Using a complete two-dimensional square-well basis set, the wave function of each individual wire subband edge with index  $\alpha$  is expanded according to

$$\Psi^{(\alpha, \text{rh})}(x, y) = \sum_{m,n} \begin{pmatrix} a_{mn}^{(\alpha, \text{rh})} \\ b_{mn}^{(\alpha, \text{rh})} \\ c_{mn}^{(\alpha, \text{rh})} \\ d_{mn}^{(\alpha, \text{rh})} \end{pmatrix} \frac{2 \sin \frac{m\pi x}{W_x} \sin \frac{n\pi y}{W_y}}{\sqrt{W_x W_y}}, \quad (12)$$

from which the hole wire eigenenergies  $E^{(\alpha, \text{rh})}$  and expansion coefficients in Eq. (12) are obtained by numerical diagonalization of  $H_L^s + V_{\text{rh}}(x, y)$  within this basis.

Similar calculations are performed for cylindrical wires confined by a harmonic potential

$$V_{\text{cs}}(x, y) = \frac{(\gamma_1 + 5\gamma_2/2)\omega^2}{2}(x^2 + y^2), \quad (13)$$

$$\Psi^{(\alpha, \text{cs})}(x, y) = \sum_{m, n} \begin{pmatrix} a_{mn}^{(\alpha, \text{cs})} \\ b_{mn}^{(\alpha, \text{cs})} \\ c_{mn}^{(\alpha, \text{cs})} \\ d_{mn}^{(\alpha, \text{cs})} \end{pmatrix} \sqrt{\frac{\omega}{\pi m! n! 2^{m+n}}} H_m(\sqrt{\omega}x) H_n(\sqrt{\omega}y) e^{-\omega(x^2+y^2)/2}. \quad (14)$$

Numerical diagonalization of  $H_L^s + V_{\text{cs}}(x, y)$  within this basis yields the corresponding eigenenergies  $E^{(\alpha, \text{cs})}$  and expansion coefficients in Eq. (14).

### III. VALENCE BAND MIXING IN HOLE NANOWIRES

#### A. Cylindrical hole wires with hard-wall confinement

We will start by analyzing the hole subband edge states in cylindrical hard-wall wires, which are of the form given in Eq. (9). To begin with, we turn our attention to the detailed form of the secular equations (10) and (11). A special case arises for subbands with  $F_z = \sigma \frac{1}{2}$ . For these values of  $F_z$ , the spinor entries in the hole-wire wave functions [Eq. (9)] are proportional to  $J_{\pm 1}(k_{\perp}^{\nu} r)$ . Since  $J_{-1}(x) = -J_1(x)$ , the secular equations reduce to  $J_1(k_{\perp}^{\nu} r) = 0$ ; a condition that can be satisfied by the individual bulk-hole eigenstates with  $\nu = \pm$  that are part of the superposition in Eq. (9). Thus, for  $F_z = \sigma \frac{1}{2}$ , the wire eigenstates are actually *pure bulk states* with  $\nu = +$  or  $\nu = -$ . Note, however, that these bulk states are still of mixed HH and LH character for finite (quantized)  $k_{\perp}$ ,<sup>55</sup> hence our labeling in terms of generic quantum number  $\nu$  and *not* in terms of HH and LH as some authors do, reserving the latter labeling strictly for states that have definite angular-momentum projections  $J_z = \pm \frac{3}{2}$  and  $J_z = \pm \frac{1}{2}$ , respectively. For any other values  $F_z = -\sigma \frac{1}{2}$  and  $|F_z| > \frac{1}{2}$  the indices of the Bessel functions appearing in Eqs. (10) and (11) are not equal and the resulting wire states are true mixtures of the bulk-hole eigenstates  $\psi_{\sigma F_z +}(r, \phi)$  and  $\psi_{\sigma F_z -}(r, \phi)$ , for a given  $\sigma$ , in order to satisfy the boundary condition set by the wire confinement.

To clarify how strong the HH-LH mixing in fact is, we will analyze the wavefunction of hole nanowire subband edges in greater detail. To be specific, we use the Luttinger parameters characteristic for GaAs<sup>74</sup> in our calculations:  $\gamma_1 = 6.98$ ,  $\gamma_2 = 2.06$ ,  $\gamma_3 = 2.93$ , hence  $\gamma_s = 2.58$ . (We remind the reader that the following results are calculated using the spherical approximation for the Luttinger Hamiltonian.). At  $B_z = 0$ , the wire eigenstates are two-fold degenerate, the degeneracy occurring between states corresponding to subspaces  $\sigma = \pm$  characterized by  $\sigma F_z$ . We will assume  $\sigma = +$  in the following

where  $\omega$  is a measure for the softness of the harmonic potential. The eigenstates of these wires are expanded in a complete basis set using Hermite polynomials according to

and suppress the index  $\sigma$  for brevity.

We illustrate the HH-LH mixing in two different ways. The traditional approach is to show the squared amplitudes of the HH and LH components in the subband eigenfunctions. However, the thus obtained HH or LH density profile depends on the chosen basis, i.e., the quantization axis of total angular momentum. As an alternative, we will also consider a quantity that measures the *invariant* hole spin-polarization density,  $P = \rho_1^2/\rho_0^2$ . Here the quantities  $\rho_1^2$  and  $\rho_0^2$  are scalar invariants derived from the spin- $\frac{3}{2}$  density matrix<sup>63</sup> that are related to the hole spin-dipole and total charge density, respectively. A pure HH state has  $P = 1.8$  everywhere, whereas a pure LH character yields  $P = 0.2$  uniformly in space. The formulation in terms of scalar invariants is basis-set independent. In principle, it therefore enables a more rigorous analysis of HH-LH mixing than would be possible in the traditional approach.

In Fig. 2, results are shown for the topmost subband edge (i.e., the subband with index  $\alpha = 1$ ). The subband-edge state is characterized by  $F_z = -\frac{1}{2}$ . Figures 2(a) and (b) give the cross-sectional profiles of the HH and LH components in the subband-edge wavefunction, illustrating that (i) the spatial density profile of the two components is very different, and

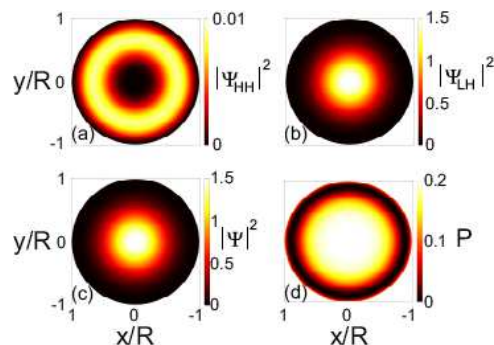


FIG. 2: (Color online) Analysis of the highest-in-energy quantum wire subband-edge state with  $\alpha = 1$  and  $F_z = -\frac{1}{2}$  (i.e.,  $\sigma = +$ ). Square amplitude of (a) the HH component and (b) the LH component of the subband edge wave function. (c) Total wavefunction amplitude squared. (d) Spatial variation of the hole spin-polarization density,  $P = \rho_1^2/\rho_0^2$ .  $P = 0.2$  corresponds to LH and  $P = 1.8$  to HH character.



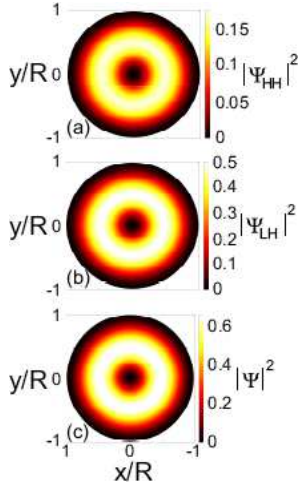


FIG. 3: (Color online) Analysis of the quantum wire subband edge with  $\alpha = 2$  and  $F_z = \frac{1}{2}$  of a cylindrical, hard-wall confined hole nanowire. Squared amplitude of the (a) HH component, and (b) LH component of the subband edge wave function. (c) Total wavefunction amplitude squared. The hole spin-polarization density,  $P$ , is zero for this subband throughout the entire crosssection of the nanowire, and is thus not shown.

(ii) their respective overall magnitudes differ by two orders of magnitude, with the LH component being the dominant one. These findings are also reflected in the (normalized) *hole-spin polarization density*,  $P$ , which is shown in Fig. 2(d). The normalization by  $\rho_0^2$  (which is a measure of the hole *charge density*) ensures that the observed spatial variations in the hole-spin polarization density can indeed be attributed to hole spin and not charge-density variations. For comparison, the charge density profile is shown in Fig. 2(c).

Inspection of the hole-spin polarization density  $P$  shows that the eigenstate is predominantly LH-like throughout most of the core of the wire, where  $P = 0.2$ . However, toward the edge, i.e., with increasing  $r$ , the hole-spin polarization *vanishes*, only to recover to a finite value at the very edge of the cylindrical confining potential. This is a manifestation of HH-LH mixing. The predominantly LH character of the topmost hole-wire subband in GaAs is in agreement with other theoretical predictions.<sup>27,54,75</sup>

We now turn our attention to the second-highest subband, with index  $\alpha = 2$ . This wire subband edge is characterized by  $F_z = \frac{1}{2}$  and therefore is actually a bulk-hole eigenstate. (See discussion above.) Figures 3(a)–3(c) show the squared amplitudes of the HH and LH components of the wavefunction, along with the total hole charge density profile. The hole-spin polarization density turns out to vanish identically across the entire crosssection of the wire and is therefore not shown. This means that the second-highest subband edge *completely* lacks spin polarization. Here the difference between the traditional approach toward discussing HH-LH mixing and the alternative one based on spin-density-matrix invariants<sup>63</sup> is most transparent. We will elaborate on this fact more later on.

The third-highest subband edge turns out to be of predominantly HH character, as can be seen from Fig. 4. The hole-

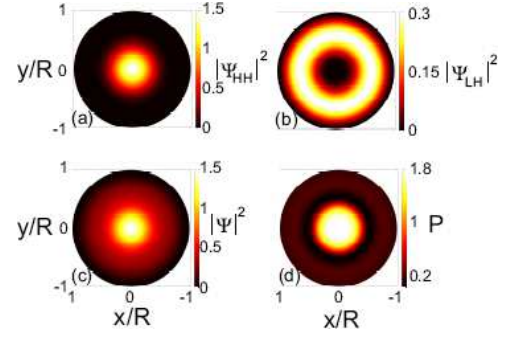


FIG. 4: (Color online) Analysis of the quantum wire subband with  $\alpha = 3$  and  $F_z = \frac{3}{2}$ . Squared amplitude of the (a) HH component, and (b) LH component of the total subband edge wave function. (c) Total wavefunction amplitude squared. (d) Spatial distribution of the hole spin-polarization density,  $P = \rho_1^2/\rho_0^2$ .

spin polarization density profile, Fig. 4(d), shows clearly that the wavefunction around the core of the wire is of purely HH character ( $P = 1.8$ ). With increasing  $r$ , however, the hole-spin polarization drops to zero, subsequently recovering values around  $P = 0.2$ , which signifies a LH character. The HH-LH mixture variations can also be seen explicitly by comparing the magnitudes and spatial profile of the square amplitudes of the HH and LH components of the wavefunction, shown in Figs. 4(a) and (b), respectively.

For subbands at decreasing energy (i.e., those with higher subband index  $\alpha$ ), the hole-spin polarization density profiles become increasingly complex. In Fig. 5 we show the hole-spin polarization density  $P$  for the subband edges with  $\alpha = 4 \dots 8$  and  $\alpha = 10$ . The subband edge with  $\alpha = 9$  has  $F_z = \frac{1}{2}$  similarly to the one with  $\alpha = 2$  and, hence, is again also a bulk-hole eigenstate with vanishing polarization across the entire wire crosssection.

The fourth-highest level ( $\alpha = 4$ ) is predominantly LH-like

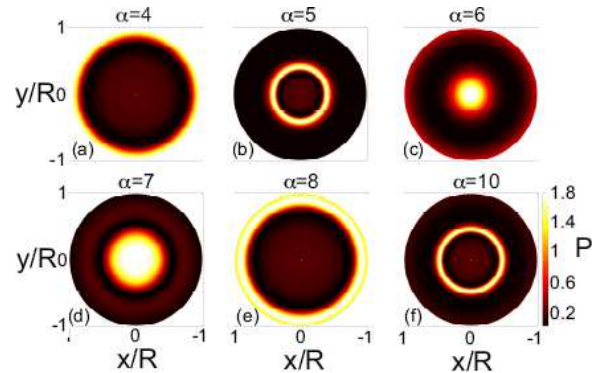


FIG. 5: (Color online) Spatial distribution of the hole spin-polarization density,  $P = \rho_1^2/\rho_0^2$ , of subband edge states with (a)  $\alpha = 4$ ,  $F_z = -\frac{3}{2}$  (b)  $\alpha = 5$ ,  $F_z = -\frac{1}{2}$  (c)  $\alpha = 6$ ,  $F_z = \frac{3}{2}$  (d)  $\alpha = 7$ ,  $F_z = \frac{5}{2}$  (e)  $\alpha = 8$ ,  $F_z = -\frac{5}{2}$  (f)  $\alpha = 10$ ,  $F_z = -\frac{3}{2}$ . The wire subband with  $\alpha = 9$  is characterized by  $F_z = \frac{1}{2}$  and has zero hole-spin polarization throughout the entire crosssection of the wire, and is thus not shown.

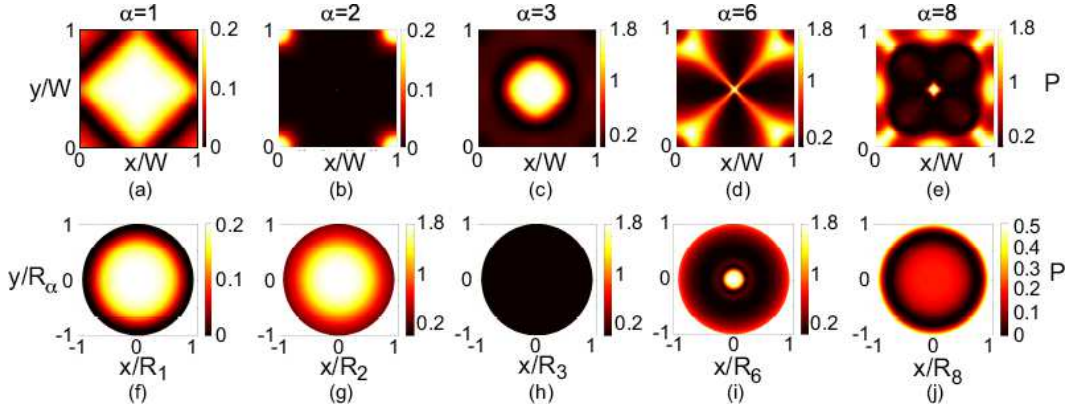


FIG. 6: (Color online) Spatial distribution of the hole spin-polarization density,  $P = \rho_1^2/\rho_0^0$  for the levels  $\alpha = 1, 2, 3, 6, 8$ , for square-crosssection hard-wall confinement (a)-(e) and cylindrical soft-wall confinement (f)-(j) hole nanowires.  $R_\alpha = [2E^{(\alpha,cs)}/(\gamma_1 + 5/2\gamma_s)]^{1/2}$ .

throughout the core of the wire. The hole-spin polarization drops to zero with increasing  $r$ , only to recover and switch to a HH character,  $P = 1.8$ , at the edge of the wire. A similar behavior is observed for the subband edge with  $\alpha = 8$ . The other subband edges show equally large variations of the hole-spin polarization as a function of the radial coordinate  $r$ . This has been found to be a general feature for all subband-edge levels characterized by  $F_z \neq \frac{1}{2}$  and is a clear manifestation of the strong valence band mixing.

### B. Dependence on shape and strength of the wire confinement

To investigate the universality of our findings, we have performed similar analysis for hole nanowires with confining potentials of different shape (or symmetry) and strength. In particular, we considered two additional cases, namely hard-wall confined hole wires with *square* crosssection, and cylindrical hole nanowires confined by a *harmonic* potential. We continue using the spherical approximation for the moment, deferring a discussion about cubic crystal-symmetry effects to later parts of the paper.

The subband edges of wires defined by the two additional types of confinement are analyzed in the same way as we did previously for the cylindrical, hard-wall confined ones. In particular, we are again focusing on the hole-spin polarization density profiles to reveal the nature of HH-LH mixing. In Fig. 6, we show the calculated hole-spin polarization density profiles,  $P$ , for square crosssection, hard-wall (upper row), and cylindrical, soft-wall hole nanowires (bottom row). For brevity, we only focus on the subband edges with  $\alpha = 1, 2, 3, 6, 8$  to illustrate our main findings.

The topmost subband with  $\alpha = 1$  is seen to be of LH character, i.e., having  $P = 0.2$ , throughout most of the wire crosssection. Especially the cylindrical wire with harmonic confining potential shows a hole-spin polarization density profile that is very similar to the corresponding hard-wall, cylindrical wire. This is not surprising, as both confining potentials are axially symmetric. For the square-crosssection wire, on the

other hand, the lower symmetry of the confining potential is reflected in the polarization density profile. Nevertheless, the predominant character of the subband edge is still LH-like, showing that this feature is indeed very robust.<sup>27,54</sup>

The second-highest subband edge (with  $\alpha = 2$ ) shows quite a different hole-spin polarization profile when comparing the different confining potentials. The square crosssection nanowire shows a vanishing polarization at the center of the wire, similar to the cylindrical hard-wall wire. However, due the reduced symmetry, the polarization is finite at the corners of the wire, where the hole-spin polarization is of LH-character. For the soft-wall cylindrical wire, the second subband displays a predominantly HH character throughout most of the nanowire crosssection. However, examining the third-highest subband edges with  $\alpha = 3$ , we see that the square crosssection, hard-wall wire state exhibits a HH-character (similar to the cylindrical hard-wall case), whereas the cylindrical soft-wall nanowire has zero polarization. Thus, a level switching in energy between the subband edges with  $\alpha = 2$  and  $\alpha = 3$  has occurred for the soft-wall cylindrical nanowire in comparison with its hard-wall cylindrical and square crosssection counterparts.

For subband edges with higher  $\alpha$ , the deviations from axial symmetry for the square crosssection wire become increasingly more prominent, as is shown explicitly for the subband edges with  $\alpha = 6$  and  $\alpha = 8$ . The soft-wall cylindrical wire on the other hand displays hole-spin polarization profiles similar to the hard-wall cylindrical case.

Quite generally, our extensive studies of the hole-spin polarization of subband edges in nanowires show that HH-LH mixing strongly affects the polarization of individual subbands, a characteristic that is universal and independent of the symmetry and shape of the confining potential. In addition, we find that the topmost subband edge states with small  $\alpha$  have HH-LH characters that are robust against changes in the confining potentials.

## IV. SPIN SPLITTING OF HOLE-WIRE SUBBAND EDGES

### A. Luttinger model for bulk holes subject to a magnetic field

We will now focus on the spin splitting of hole nanowire states in the presence of a magnetic field applied parallel to the wire axis. The external field couples to both the spin-3/2 and orbital degrees of freedom. The Zeeman Hamiltonian describing the interaction between the magnetic field,  $B_z$ , and the spin degree of freedom is given by

$$H_Z = -2\kappa\mu_B B_z \cdot \hat{J}_z, \quad (15)$$

where  $\mu_B$  is the Bohr magneton and  $\kappa$  is the bulk hole  $g$  factor.<sup>39</sup> We will neglect the anisotropic Zeeman contribution

---


$$H_{\text{orb}}^s = H_{\text{orb,diag}}^s + H_{\text{orb,mix}}^s = - \left[ \gamma_1 \cdot \mathbb{1}_{4 \times 4} + \gamma_s \left( \hat{J}_z^2 - \frac{5}{4} \cdot \mathbb{1}_{4 \times 4} \right) \right] \hat{L}_z \mu_B B_z - i\gamma_s \left( \hat{x}_- \hat{k}_- \hat{J}_+^2 - \hat{x}_+ \hat{k}_+ \hat{J}_-^2 \right) \mu_B B_z. \quad (16)$$


---

The first term is proportional to the orbital angular momentum operator  $\hat{L}_z$  and is diagonal in spin space. We denote this contribution by  $H_{\text{orb,diag}}^s$ . The remaining terms are off-diagonal in spin space, coupling states with  $J_z$  eigenvalue differing by 2. We denote this contribution by  $H_{\text{orb,mix}}^s$ . These two contributions will be analyzed in greater detail in our discussion of the orbital contribution to the total  $g$  factor of hole nanowire subband edges.

At zero magnetic field, subbands with a given  $\alpha$  and  $\sigma F_z$  are doubly degenerate. A finite  $B_z$  lifts this degeneracy, giving rise to a spin splitting from which we extract a  $g$  factor according to

$$g_{\text{tot}}^\alpha = \lim_{B_z \rightarrow 0} \text{sgn}(\langle \hat{F}_z \rangle_\alpha^+) \frac{E_\alpha^+(B_z) - E_\alpha^-(B_z)}{\mu_B B_z}. \quad (17)$$

The sign factor introduces the physical definition of assigning sign according to the projection of  $\langle \hat{\mathbf{F}} \rangle$  along the magnetic field direction. It removes any ambiguity relating to the particular choice of symmetry,  $\sigma$ , labelling the  $2 \times 2$  blocks of the Hamiltonian. Due to the finite energy separation between wire subbands, this definition is equivalent to the perturbative (in  $B_z$ ) result

$$\begin{aligned} g_{\text{tot}}^\alpha &= \text{sgn}(\langle \hat{F}_z \rangle_\alpha^+) \frac{\langle H_Z + H_{\text{orb}}^s \rangle_\alpha^+ - \langle H_Z + H_{\text{orb}}^s \rangle_\alpha^-}{\mu_B B_z}, \\ &\equiv \text{sgn}(\langle \hat{F}_z \rangle_\alpha^+) \frac{2\langle H_Z + H_{\text{orb}}^s \rangle_\alpha^+}{\mu_B B_z}, \end{aligned} \quad (18)$$

where the expectation values are taken with respect to the  $B_z = 0$  wire subband edge eigenstates with  $\sigma = +$ .

In the following, we analyze the individual bulk-material and orbital contributions to the total  $g$  factor  $g_{\text{tot}}^\alpha = g_Z^\alpha + g_{\text{orb,diag}}^\alpha + g_{\text{orb,mix}}^\alpha$  that arise from the linear-in- $B_z$  terms  $H_Z$ ,

that is of higher order in  $\mathbf{J}$  because, in typical semiconductors and for the crystallographic wire direction we consider, it is much smaller than the one given in Eq. (15).

In order to include the orbital effects due to a magnetic field applied in the  $z$  direction, we replace  $\hat{\mathbf{k}} \rightarrow \hat{\mathbf{k}} + e\mathbf{A}$ . The symmetric gauge  $\mathbf{A} = (-\frac{y}{2}, \frac{x}{2}, 0)B_z$  will be used, and we will only consider resulting terms linear in  $B_z$  because we extract  $g$  factors from the small-magnetic-field limit. In the spherical approximation, i.e., using the Luttinger Hamiltonian of Eq. (2), the orbital terms arising from the replacement of canonical wavevector with the kinetic one have the following form (we use atomic units and the definitions  $\hat{L}_z = x\hat{k}_y - y\hat{k}_x$  and  $\hat{x}_\pm = x \pm iy$ )

$H_{\text{orb,diag}}^s$ , and  $H_{\text{orb,mix}}^s$ , respectively. It is useful to understand each contribution's separate properties, as their relative importance may vary depending on physical details. For example, the bulk-material contribution  $g_Z^\alpha$  will dominate in diluted magnetic semiconductor wires where  $\kappa$  can be enhanced by several orders of magnitude due to the  $p$ - $d$  exchange interaction between hole carriers and magnetic dopant ions.<sup>60,76</sup>

### B. Bulk-material contribution to $g$ factors

We begin by analyzing the contribution to  $g_{\text{tot}}^\alpha$  that is due to the Hamiltonian  $H_Z$ . It follows from Eqs. (18) and (15) that the  $g$  factor derived from the bulk-hole Zeeman effect has the form

$$g_Z^\alpha = -4\kappa \text{sgn}(\langle \hat{F}_z \rangle_\alpha^+) \langle \hat{J}_z \rangle_\alpha^+ = -2\sqrt{5}\kappa \text{sgn}(\langle \hat{F}_z \rangle_\alpha^+) \rho_{10}. \quad (19)$$

In the r.h.s equality, we have expressed  $g_Z^\alpha$  in terms of  $\rho_{10}$ , which is a dipole-related component of the spin-3/2 density matrix (defined in Table III of Ref. 63).

It is clear from Eq. (19) that an eigenstate of pure HH character has an effective  $g$  factor of  $-6\kappa$ , while a pure LH state has a spin splitting characterized by  $g = -2\kappa$ . This is certainly the case for bulk-hole states at the valence-band edges.<sup>39</sup> The situation is different for quantum-confined hole states, e.g., in a wire.<sup>51,55</sup> As discussed in Sec. III, strong HH-LH mixing is a universal characteristic of hole nanowire subband edges, and hole nanowire states of purely HH or LH character are not expected to be found. In particular, the analysis of the squared amplitude of the spin-3/2 dipole moment in Sec. III showed that the normalized hole-spin polarization profiles,  $P = \rho_1^2/\rho_0^2$  display strong spatial variations as a manifestation of HH-LH mixing. ( $\rho_1$  is directly related to  $\rho_{10}$ ; see



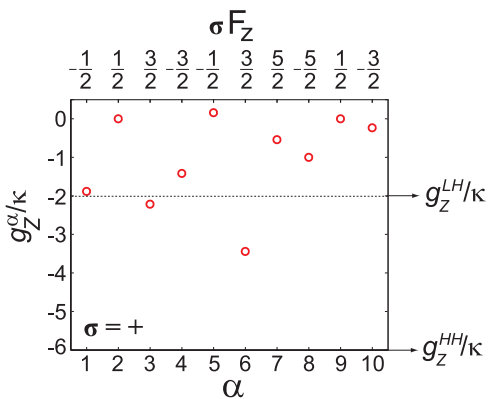


FIG. 7: (Color online) Bulk-material contribution to the  $g$ -factor of the highest-in-energy subband-edge states, with  $\alpha = 1 \dots 10$ , of a hole nanowire defined by a cylindrical hard-wall confinement. The arrows indicate the values of  $g_Z/\kappa = -2$  and  $-6$  corresponding to the bulk-hole  $g$ -factor of pure LH and HH states, respectively.

Ref. 63 for details.) The question is thus: To what extent does the HH-LH mixing change the  $g$  factors for hole states in a wire as compared with the bulk-material (HH and LH) values of  $-6\kappa$  and  $-2\kappa$ ?

Figure 7 shows the effective  $g$  factors normalized by  $\kappa$ , of the ten highest subband edges in cylindrical nanowires with hard-wall confinement. The values display strong variations as a function of subband index  $\alpha$ . Furthermore, most subbands have values that are strongly suppressed in comparison to the values expected for pure HH and LH states, respectively. Inspection of the hole-spin density profiles discussed in Sec. III and comparison with the  $g$ -factor values shows a strong correlation, establishing a direct connection between HH-LH mixing and the observed large  $g$ -factor variations as a function of subband index. For example, the topmost subband edge ( $\alpha = 1$ ) was found to be predominantly of LH character (see Fig. 2). Correspondingly, its  $g$  factor is found to be close to  $-2\kappa$ , just as expected from Eq. (19) for a pure LH state.

The second (and ninth) subband edges from the top have vanishing polarizations, which correlates with a vanishing  $g$  factor. Both the second and the ninth state belong to the class of subband edges with  $F_z = \frac{1}{2}$  and are thus also a bulk-hole eigenstate. As discussed in Fig. 2 of Ref. 55, the spin splitting of bulk hole bands is characterized at high values of  $k_\perp$  by values of  $g = 0$  or  $|g| = 4\kappa$ . The subbands with  $\alpha = 2$  and  $\alpha = 9$  are examples of the former type. We have also found wire-subband edges of the other type whose spin splitting is characterized by  $|g| = 4\kappa$ , e.g., the one with  $\alpha = 16$ .

The dipole moment turns out to be just one of three non-trivial multipole moments that characterize a spin-3/2 state.<sup>63</sup> This is a fundamental difference with a spin-1/2 system where the dipole moment suffices to uniquely determine the spin state. When the spin-3/2 polarization (i.e., the dipole moment) vanishes for pure spin states in two-dimensional<sup>63</sup> and one-dimensional<sup>55</sup> hole systems, a substantial *octupole* moment can exist. For hole nanowire subband edges, a mathematical

TABLE I: Bulk-material contribution to  $g$ -factors for hole nanowire subband-edges with index  $\alpha = 1 \dots 10$  for three different types of wire confinement: (i) hard-wall cylindrical cross-section, (ii) hard-wall square cross-section, and (iii) soft-wall cylindrical cross-section.

$\alpha$	1	2	3	4	5	6	7	8	9	10
(i) $g_Z^\alpha$	-2.26	0.00	-2.66	-1.70	0.19	-4.13	-0.65	-1.20	0.00	-0.28
(ii) $g_Z^\alpha$	-2.22	0.07	-3.39	-1.55	0.06	-2.58	-0.72	-0.59	0.08	-0.17
(iii) $g_Z^\alpha$	-1.84	-5.57	0.00	-1.34	-0.66	-1.60	-2.68	-0.97	0.01	-0.94

relation<sup>55</sup> illustrates this point:

$$\rho_0^2 = 2\rho_2^2 = \rho_1^2 + \rho_3^2 \quad . \quad (20)$$

Equation (20) links the scalar invariants  $\rho_i^2$  obtained from the multipole-like expansion of the spin-3/2 density matrix.<sup>63</sup> The squared monopole,  $\rho_0^2$ , and dipole,  $\rho_1^2$ , correspond (apart from prefactors) to the squared magnitude of the hole charge density and hole-spin polarization density, respectively. The quadrupole and octupole are unique to spin-3/2 systems. The quadrupole is a measure of the HH-LH mixing, while the octupole does not have a straightforward physical interpretation. The left equality in Eq. (20) quantifies the HH-LH mixing that is present at subband edges. The right-hand equality implies that the hole-spin polarization, measured by the dipole moment  $\rho_1$ , and the octupole,  $\rho_3$ , are complementary. Thus, for the subband edges for which the hole-spin polarization vanishes, a maximum octupole moment is induced. Similar comparisons can be made for all the wire eigenstates. In general, states with mainly HH (LH) character will have  $g$  factors close to  $-6\kappa$  ( $g = -2\kappa$ ). States with mixed character, displaying fluctuations in the hole-spin polarization profiles, have widely varying values for  $g$ .

In Table I the calculated values of the  $g$  factors (with  $\kappa = 1.2$ , the value<sup>39</sup> corresponding to GaAs) for hole wires with square-cross-section hard-wall confinement (mid-row) and cylindrical harmonic potential (bottom row) are shown along with the numerical values for the  $g$ -factors corresponding to Fig. 7 for the cylindrical hard-wall nanowire (top row). In general, we observe strong similarities between the  $g$ -factors of the different structures, with respect to both magnitude and sign. This is especially clear at low energies, where the axial symmetry seems to be retained even in the wire with square cross-section. These findings do not come as a surprise when one considers the similarity of hole-spin polarization density profiles for the low-lying subband edges (shown in Fig. 6). As could be expected, the similarity is stronger for the two types of cylindrical confinement, while the square-cross-section wire states display some complex hole-spin polarization variations (e.g., for subband edges with  $\alpha = 6$  and 8), with corresponding discrepancies between the calculated  $g$  factor values of the square cross-section wire and the corresponding cylindrical ones. Note also that the subband edges with vanishing polarization in the cylindrical wires, acquire a finite, albeit small, polarization for the square cross-section one, with a corresponding non-zero value of the hole  $g$  factor. Another interesting observation is the level switching that occurs between subband edges with  $\alpha = 2$  and 3 for the cylindrical wire with

TABLE II: Total orbital  $g$  factors,  $g_{\text{orb}}^{\alpha}$ , and the individual contributions  $g_{\text{orb,diag}}^{\alpha}$  and  $g_{\text{orb,mix}}^{\alpha}$  for the ten highest subband edges with  $\alpha = 1 \dots 10$  in cylindrical hardwall hole nanowires.

$\alpha, \sigma F_z$	$1, -\frac{1}{2}$	$2, \frac{1}{2}$	$3, \frac{3}{2}$	$4, -\frac{3}{2}$	$5, -\frac{1}{2}$	$6, \frac{3}{2}$	$7, \frac{5}{2}$	$8, -\frac{5}{2}$	$9, \frac{1}{2}$	$10, -\frac{3}{2}$
$g_{\text{orb}}^{\alpha}$	2.78	-1.82	4.91	-0.05	-8.62	-14.10	-4.46	-3.28	-1.82	-18.09
$g_{\text{orb,diag}}^{\alpha}$	-0.54	-1.82	-8.27	-12.40	-10.33	-5.66	-24.10	-25.04	-1.82	-19.63
$g_{\text{orb,mix}}^{\alpha}$	3.32	0.00	13.18	12.35	1.71	-8.44	19.64	21.76	0.00	1.54

parabolic confining potential. This is an example for the sensitivity of physical quantities (here the wire bound-state energy) with respect to quantum-confinement-induced HH-LH mixing.

We conclude that, as a universal characteristic of hole nanowires, states are of mixed HH and LH character even at the subband edges. This is manifested by large variations in the bulk-material contribution to  $g$  factors as a function of subband index, concomitant with an overall suppressed magnitude of Zeeman splitting as compared with free holes.

### C. Orbital effects

We now turn our attention to how the coupling between the holes' orbital degrees of freedom and the magnetic field affects the splitting of hole-nanowire subband edges in a magnetic field applied parallel to the wire axis. Using a similar perturbation approach as in Sec. IV B, the orbital contribution to the total  $g$ -factor for a subband edge with index  $\alpha$  can be written as

$$g_{\text{orb}}^{\alpha} = g_{\text{orb,diag}}^{\alpha} + g_{\text{orb,mix}}^{\alpha} , \quad (21)$$

where

$$g_{\text{orb,diag}}^{\alpha} = \frac{-2 \left[ \gamma_1 \langle \hat{L}_z \mathbb{1}_{4 \times 4} \rangle_{\alpha}^{+} + \gamma_s \langle (\hat{J}_z^2 - \frac{5}{4} \mathbb{1}_{4 \times 4}) \hat{L}_z \rangle_{\alpha}^{+} \right]}{\text{sgn}(\langle \hat{F}_z \rangle_{\alpha}^{+})} \quad (22)$$

$$g_{\text{orb,mix}}^{\alpha} = \frac{-2\gamma_s}{\text{sgn}(\langle \hat{F}_z \rangle_{\alpha}^{+})} \langle i\hat{x}_- \hat{k}_- \hat{J}_+^2 - i\hat{x}_+ \hat{k}_+ \hat{J}_-^2 \rangle_{\alpha}^{+} .$$

The total orbital  $g$ -factor contribution  $g_{\text{orb}}^{\alpha}$  is shown in Table II (top row) for the ten highest-in-energy subband edges ( $\alpha = 1 \dots 10$ ), of a cylindrical hard-wall wire. The orbital  $g$  factor displays large variations as a function of subband index  $\alpha$ . Moreover, for some subband indices, e.g.,  $\alpha = 6$  and  $10$ , the values are significantly larger than the corresponding bulk-material contributions discussed in the previous subsection. In general, we observe that the orbital contribution to the total  $g$  factor of hole subband edges in cylindrical nanowires dominates over the corresponding bulk-material contributions.

Examining the individual contributions  $g_{\text{orb,diag}}^{\alpha}$  and  $g_{\text{orb,mix}}^{\alpha}$ , we see that, first of all, the two contributions have similar magnitudes. In addition, the two contributions have in general opposite sign, with the exception of that for the subband edge with  $\alpha = 6$ . The overall sign of the orbital  $g_{\text{orb}}^{\alpha}$  is thus determined by the competition between these two terms.

The origin of large fluctuations in the total orbital contribution to the  $g$  factor can be understood by examining the interplay between the diagonal and mixing terms in greater detail for cylindrical hard-wall hole wires. The operators entering Eqs. (22) and (23) can be expressed in polar coordinates as

$$\begin{aligned} \hat{L}_z &= -i\partial_{\phi} , \\ \hat{x}_- \hat{k}_- &= -i\hat{L}_-^2 (r\partial r + \hat{L}_z) , \\ \hat{x}_+ \hat{k}_+ &= (\hat{x}_- \hat{k}_-)^{\dagger} , \\ \hat{L}_- &= e^{-i\phi} . \end{aligned} \quad (24)$$

Using the wire eigenstates shown in Eq. (9) it follows that, in the limit  $B_z \rightarrow 0$ , the contribution of  $H_{\text{orb,diag}}^s$  to the orbital (23) factor is given by

$$g_{\text{orb,diag}}^{\alpha} = -2 \text{sgn}(\langle \hat{F}_z \rangle_{\alpha}^{+}) \left[ \left( F_z - \frac{3}{2} \right) (\gamma_1 + \gamma_s) \left\langle \frac{3}{2} \middle| \frac{3}{2} \right\rangle_{\alpha}^{+} + \left( F_z + \frac{1}{2} \right) (\gamma_1 - \gamma_s) \left\langle -\frac{1}{2} \middle| -\frac{1}{2} \right\rangle_{\alpha}^{+} \right] , \quad (25)$$

where the angular brackets  $\langle \frac{3}{2} | \frac{3}{2} \rangle$  and  $\langle -\frac{1}{2} | -\frac{1}{2} \rangle$  are squared amplitudes of the HH and LH components of an eigenstate  $\psi_{+F_z}^{(\alpha, \text{ch})}$  as described in Eq. (9). Equation (25) is linear in  $F_z$ , reflecting the angular momentum that is acquired by the envelope wave function of the hole subband edge due to the cylindrical symmetric quantum confinement. We also note that the two terms in Eq. (25) differ by a factor of  $\gamma_1 \pm \gamma_s$ . This is a manifestation of HH-LH *splitting*.

In Fig. 8(a), we show values of  $g_{\text{orb,diag}}^{\alpha}$  for subband edges with different  $F_z$ . For each value of  $F_z$ , the four  $g$ -factor values correspond to the four highest-in-energy subband edges with that particular  $F_z$ . We label this sequence in energy by the index  $\beta$ , not to be confused with the general subband index  $\alpha$ . A linear dependence in  $F_z$  can be clearly seen from the figure, confirming the presence of the large quantum-confinement-induced envelope angular momentum. We also

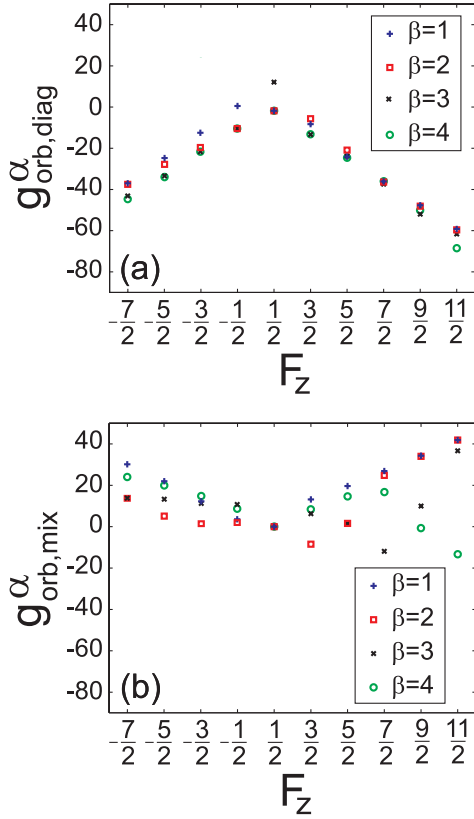


FIG. 8: (Color online) Values for individual orbital  $g$ -factor contributions (a)  $g_{\text{orb,diag}}^{\alpha}$  and (b)  $g_{\text{orb,mix}}^{\alpha}$  for subband edges with  $-\frac{7}{2} \leq F_z \leq \frac{11}{2}$  (for the  $\sigma = +$  states) in a cylindrical hard-wall hole nanowire. The index  $\beta$  labels subband edges with a given  $F_z$  in order of decreasing energy.

observe a spread in the  $g$ -factor values for a fixed value of  $F_z$  corresponding to different energies (and subband index  $\alpha$ ). This is a clear manifestation of HH-LH mixing, which enters through the squared amplitudes of the HH and LH components in Eq. (25). Thus, even though the Hamiltonian giving rise to the splitting characterized by  $g_{\text{orb,diag}}^{\alpha}$  is diagonal in spin-space, its contribution to the spin splitting is affected by the quantum-confinement-induced HH-LH mixing in the unperturbed states. The fluctuations in  $g_{\text{orb,diag}}^{\alpha}$  as a function of subband index  $\alpha$  are therefore due to the different subbands having different total angular momentum  $F_z$ , as well as different HH-LH character.

In contrast to  $H_{\text{orb,diag}}^s$ , the Hamiltonian  $H_{\text{orb,mix}}^s$  couples hole subband edge wave function components with different  $J_z$ . Thus, it gives rise to HH-LH mixing that is in addition to the HH-LH mixing inherent to the unperturbed wire eigenstates discussed in Sec. III. For a cylindrical hard-wall hole wire, this generates a contribution to the spin splitting given by

$$g_{\text{orb,mix}}^{\alpha} = \frac{-4\sqrt{3}}{\text{sgn}(\langle \hat{F}_z \rangle_{\alpha}^+)} \left\langle \frac{3}{2} \left| \hat{L}_-^2 (r\partial_r + \hat{L}_z) \right| - \frac{1}{2} \right\rangle_{\alpha}^+ . \quad (26)$$

Here the notation indicates that the expectation value is be-

tween HH and LH components of the subband edge state with  $\alpha$  and  $+F_z$ , with spin projections  $J_z = 3/2$  and  $J_z = -1/2$ , respectively.

In Fig. 8(b), we show the  $g$ -factor contributions  $g_{\text{orb,mix}}^{\alpha}$  for subband edges with  $-\frac{7}{2} \leq F_z \leq \frac{11}{2}$ . Again, for each value of  $F_z$  we show the calculated  $g$  factor values for the four highest-in-energy subband edges with the given  $F_z$ . While the characteristics of the mixing term are more complicated, we can discern some general trends. For instance, for the lowest-in-energy subband edges, with  $\beta = 1$ , a clear linear dependence on  $F_z$  is seen in the  $g$  factors. However, these  $g$  factors increase monotonically with  $|F_z|$ , in contrast to the splitting term,  $g_{\text{orb,diag}}^{\alpha}$ , which is monotonically decreasing with  $|F_z|$ . In general, the terms  $g_{\text{orb,diag}}^{\alpha}$  and  $g_{\text{orb,mix}}^{\alpha}$  have similar magnitudes but opposite sign. However, for higher energies, this general rule does not apply and a large spread between the  $g$  factors for a given  $F_z$  at different energies can be observed.

A comparison between the orbital contribution to  $g$  factors  $g_{\text{orb}}^{\alpha}$  calculated for our three model hole nanowire structures is shown in Table III. Interestingly, with the exceptions of the levels with  $\alpha = 2$  and 3, all nanowires have very similar orbital  $g$  factors for low-index levels (small  $\alpha$ ). This is true both for the magnitude and the overall sign of  $g_{\text{orb}}^{\alpha}$ . In particular, the square-cross-section wire displays similar values to the cylindrical ones, despite the lower symmetry of the confining potential. Closer inspection of the levels with  $\alpha = 2$  and 3 also shows that, in fact, the similarities extend to these levels as well, if one interchanges the values for  $\alpha = 2$  and 3 for the cylindrical wire with harmonic confinement. This is in agreement with our previous discussion on the level switching observed in the hole-spin polarization of these levels for this wire confinement potential; see Sec. III. The spread between  $g_{\text{orb}}^{\alpha}$  factors with given  $\alpha$  corresponding to different confining potentials increases, however, with increasing subband index  $\alpha$ , in accordance with the expectation that the more strongly delocalized wave functions probe the outer edges of the confining potential.

### D. Cubic corrections

Next we consider the influence of corrections due to cubic crystal symmetry. These corrections depend on the orientation of the wire with respect to crystallographic axes. In the following, we assume that the wire and, hence, the spin-3/2 quantization axis, are parallel to the [001] direction. Starting from the full Luttinger Hamiltonian  $H_L$  shown in Eq. (1), we perform the transformation  $\hat{k} \rightarrow \hat{k} + e\mathbf{A}$  in the symmetric

TABLE III: Total orbital  $g$  factors,  $g_{\text{orb}}^{\alpha}$ , for the ten highest subband edges ( $\alpha = 1 \dots 10$ ) in (i) cylindrical hard-wall, (ii) square hard-wall, and (iii) cylindrical soft-wall hole nanowires.

$\alpha$	1	2	3	4	5	6	7	8	9	10
(i) $g_{\text{orb}}^{\alpha}$	2.78	-1.82	4.91	-0.05	-8.62	-14.10	-4.46	-3.28	-1.82	-18.09
(ii) $g_{\text{orb}}^{\alpha}$	2.74	-2.21	5.88	-0.69	-6.26	-12.12	-2.39	-1.66	-1.91	-9.26
(iii) $g_{\text{orb}}^{\alpha}$	3.39	5.88	-1.82	-1.13	-3.38	-9.55	-1.81	-4.67	-1.66	-6.85

gauge. This yields the following terms linear in  $B_z$ :

$$H_{\text{orb}} = - \left\{ \left[ \gamma_1 \cdot \mathbb{1}_{4 \times 4} + \gamma_2 \left( \hat{J}_z^2 - \frac{5}{4} \cdot \mathbb{1}_{4 \times 4} \right) \right] \hat{L}_z + \gamma_2 \left( y \hat{k}_x + x \hat{k}_y \right) \left( \hat{J}_+^2 + \hat{J}_-^2 \right) + i \gamma_3 \left( x \hat{k}_x - y \hat{k}_y \right) \left( \hat{J}_+^2 - \hat{J}_-^2 \right) \right\} \mu_B B_z. \quad (27)$$

In contrast to Eq. (16), the orbital Hamiltonian of Eq. (27) contains terms proportional to  $\gamma_2$  and  $\gamma_3$ . The fact that  $\gamma_2 \neq \gamma_3$  accounts for bandwarping effects.

In Fig. 9, we show the calculated values for  $g_{\text{tot}}^\alpha$  for the hole wire subband edges with  $\alpha = 1 \dots 10$  of a square cross-section hard-wall nanowire. The open symbols are values obtained from the numerical diagonalization of  $H_L^s + H_Z + H_{\text{orb}}^s + V_{\text{rh}}(x, y)$ , i.e., using the spherical approximation for the Luttinger Hamiltonian. The filled symbols are obtained by diagonalizing  $H_L + H_Z + H_{\text{orb}} + V_{\text{rh}}(x, y)$ , which includes band warping due to the cubic crystal symmetry. For subband edges with low values of  $\alpha$ , the  $g$  factors obtained from the two approaches turn out to be very similar. For higher values of  $\alpha$ , on the other hand, we observe an increasing spread between the  $g$ -factor values corresponding to the two cases. Properties of wires aligned parallel to crystallographic directions with lower symmetry than [001] can be expected to be more strongly affected by band-warping corrections.<sup>40</sup>

### E. Interplay of bulk-material and orbital wire-bound-state contributions to $g$ factors: Tunability of sign and magnitude

We now discuss in greater detail the interplay between the various contributions to the total nanowire-hole  $g$  factor. Lets recall that  $g_{\text{tot}}^\alpha$  is the sum of three terms,  $g_{\text{tot}}^\alpha = g_Z^\alpha + g_{\text{orb,diag}}^\alpha + g_{\text{orb,mix}}^\alpha$ , which are the bulk-material, diagonal-in-

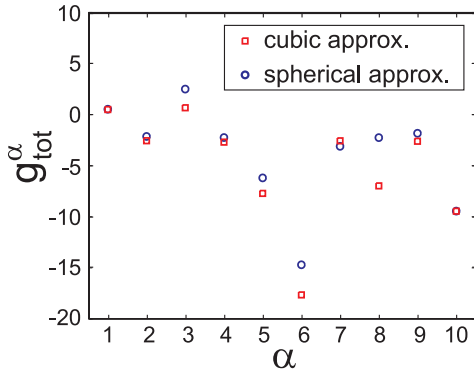


FIG. 9: Hole  $g$  factors  $g_{\text{tot}}^\alpha$  for the top ten subband edges ( $\alpha = 1 \dots 10$ ) of a square-cross-section hard-wall nanowire. Circles correspond to values obtained from diagonalizing  $H_L^s + H_{\text{orb}}^s + H_Z + V_{\text{rh}}(x, y)$ , i.e., using the spherical approximation for the Luttinger Hamiltonian.<sup>70</sup> Squares denote the values obtained from numerically diagonalizing  $H_L + H_{\text{orb}} + H_Z + V_{\text{rh}}(x, y)$ , i.e., using the Luttinger Hamiltonian reflecting the cubic crystal symmetry.

spin-space orbital, and HH-LH mixed orbital contributions, respectively. In Table IV, we show the calculated  $g_{\text{tot}}^\alpha$  and its components for the ten highest subband edges in hole nanowires with square-cross-section hard-wall quantum confinement. The values are obtained by numerical diagonalization of  $H_L + H_{\text{orb}} + H_Z + V_{\text{rh}}(x, y)$ , i.e., using the Luttinger Hamiltonian with cubic (not spherical) symmetry.

Table IV illustrates several of our main conclusions. The bulk-material contribution shows strong variations in sign and magnitude as a function of subband index. This is a manifestation of HH-LH mixing at hole-nanowire subband edges. Similar fluctuations occur for the orbital contributions. This is in part due to the fact that the envelope function of subbands with different  $\alpha$  acquire different quantum-confinement-induced orbital bound-state angular momenta. In addition, the fluctuations also originate from HH-LH mixing. The two orbital contributions  $g_{\text{orb,diag}}^\alpha$  and  $g_{\text{orb,mix}}^\alpha$  have, in general, comparable magnitudes but opposite sign.

Most importantly, the total  $g$  factor  $g_{\text{tot}}^\alpha$  depends sensitively on the relative sign and magnitude of the three contributions. As both the orbital contribution to the spin splitting and the detailed form of the HH-LH mixing depend on the details of the quantum confinement,<sup>56</sup> we expect that the interplay between the bulk-material and orbital  $g$ -factor terms can be tuned by confinement engineering. This would enable the use of nanowires to realize devices for nanospintronics. In Fig. 10 we demonstrate such tunability of hole  $g$  factors in nanowires. The thick curves show  $g_{\text{tot}}^\alpha$  for the three highest-in-energy subband edges of rectangular-cross-section hard-wall confined wires plotted as a function of the aspect ratio  $A = W_x/W_y$ . The bulk-material and orbital contributions are also shown (by the thin solid and dashed lines, respectively). A general characteristic that is observed for all three subband edges is that the total  $g$  factor approaches zero in the limit of large aspect ratio  $A$ . This is due to the fact that, with increasing  $A$ , our nanowire system approaches the 2D limit, essentially mimicking a quantum well subject to an in-plane magnetic field. For such a system, the topmost hole-quantum-well subband edge is known to have a small (within the spherical approximation: vanishing)  $g$  factor,<sup>39,40</sup> in agreement with our findings. The sudden sign change observed in  $g^2$  and  $g^3$  occurs at anticrossing points in the energy spectrum where  $\langle \hat{F}_z \rangle$  goes through zero, and consequently reverses sign.

The observed dependence of the subband edge  $g$  factor values on the aspect ratio of the confining potential is quite intriguing. All subband edges display a strong tunability of the magnitude of the  $g$  factor with a change in the aspect ratio. For the third subband, a variation of  $A$  between 1 and 2

TABLE IV: Total  $g$  factor  $g_{\text{tot}}^\alpha = g_Z^\alpha + g_{\text{orb,diag}}^\alpha + g_{\text{orb,mix}}^\alpha$  for the ten highest-in-energy subband edges ( $\alpha = 1 \dots 10$ ) of a square-cross-section hole nanowire with hard-wall confinement.  $g_Z^\alpha$  is the bulk-material contribution, which arises from the Zeeman effect of holes in the semiconductor material. The additional spin splitting due to coupling of the applied magnetic field to the orbital wire bound state is embodied in  $g_{\text{orb,diag}}^\alpha$  and  $g_{\text{orb,mix}}^\alpha$ , which are derived from the first and second terms in Eq. (27), respectively. Values shown are obtained by numerically diagonalizing the cubic Hamiltonian  $H_L + H_{\text{orb}} + H_Z + V_{\text{rh}}(x, y)$  and considering the spin splitting for  $B_z \rightarrow 0$ .

$\alpha$	1	2	3	4	5	6	7	8	9	10
$g_{\text{tot}}^\alpha$	0.50	-2.55	0.67	-2.69	-7.71	-17.64	-2.56	-6.97	-2.61	-9.45
$g_Z^\alpha$	-2.13	-0.23	-4.83	-1.33	0.55	-1.74	-1.20	-0.56	-0.13	-0.73
$g_{\text{orb,diag}}^\alpha$	-0.58	-2.35	-3.08	-12.80	-10.87	-11.09	-18.89	-25.99	-7.16	-31.20
$g_{\text{orb,mix}}^\alpha$	3.20	0.03	8.58	11.45	2.61	-4.81	17.52	19.58	4.68	22.47

gives rise to a change in the *sign* of the  $g$  factor that is not associated with an anticrossing, thus demonstrating the ability to gradually tune the spin splitting to zero. The possibility to manipulate both the magnitude and sign of  $g$  factors is a useful ingredient for spintronics applications. We therefore propose that hole nanowires may be versatile building

blocks for nanospintronics due to the demonstrated tunability that arises from the interplay between bulk-material and orbital spin splittings in an applied magnetic field. Confinement engineering of nanowires and quantum point contacts can be readily achieved with present-day technologies, e.g., using side gates on lithographically defined quantum wires<sup>66</sup> and quantum point contacts,<sup>41,42</sup> or wrap-gated self-assembled nanowires.<sup>64,65</sup>

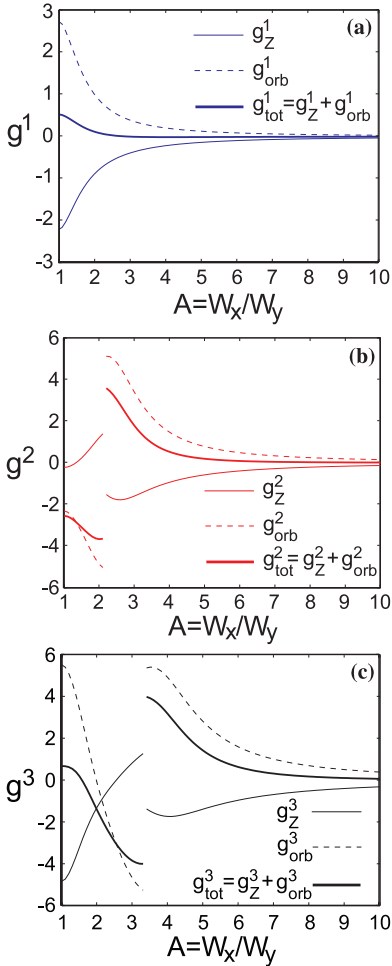


FIG. 10: Dependence of subband-edge  $g$  factors  $g_{\text{tot}}^\alpha$  on the aspect ratio  $A$  for a rectangular-cross-section hard-wall-confined nanowire (thick solid curves). We show results for the top three hole-wire subband edges: (a)  $\alpha = 1$ , (b)  $\alpha = 2$ , and (c)  $\alpha = 3$ . The thin solid and dashed curves are plots of the corresponding bulk-material and orbital contributions,  $g_Z^\alpha$  and  $g_{\text{orb}}^\alpha$ , respectively.

## F. Hole nanowire dispersions for finite $k_z$

We finish our analysis by discussing the energy dispersion of hole nanowire states due to motion along the wire direction. For finite  $k_z$ , the decomposition shown in Eq. (3) is no longer possible. Instead, the full  $4 \times 4$  Luttinger Hamiltonian must be considered. We diagonalized numerically the Hamiltonian consisting of the sum of  $H_L$  shown in Eq. (1) and  $V_{\text{rh}}(x, y)$  for a square-cross-section hard-wall GaAs nanowire oriented along the  $[001]$  direction.

The highest hole-nanowire subband dispersions are shown in Fig. 11. Several observations can be made. First, the hole dispersions are strongly non-parabolic, which is a distinct manifestation of the SO coupling and HH-LH mixing in the valence band of typical semiconductors. Second, some subbands display electron-like dispersions as well as off-center ( $k_z \neq 0$ ) maxima. For example, the highlighted points A, B, and D correspond to off-center maxima for the subbands with  $\alpha = 3, 4$  and  $8$ , respectively. The occurrence of subband edges away from the zone center, as well as the strong non-parabolic dispersions, will have direct implications for the transport and optical properties of hole nanowires.

One example is the quantized conductance of one-dimensional systems. It is well known that transport measurements in the linear-response regime of one-dimensional quantum wires and quantum point contacts yield quantized conductance steps<sup>66,77,78</sup> if the transport is ballistic. Such conductance steps occur whenever a one-dimensional subband is opened as a channel for conduction, as it falls below the electrochemical potential determined by the contacts. Typically, top or side gate are employed to adjust the wire width and, thus, the quasi-1D subband energies. In the absence of a magnetic field, the conductance steps occur in units of  $2e^2/h$ .

In Fig. 11(b), we show a schematics of the linear-response conductance of a hole nanowire with the dispersion shown in Fig. 11(a). The abscissa refers to a gate voltage applied to a



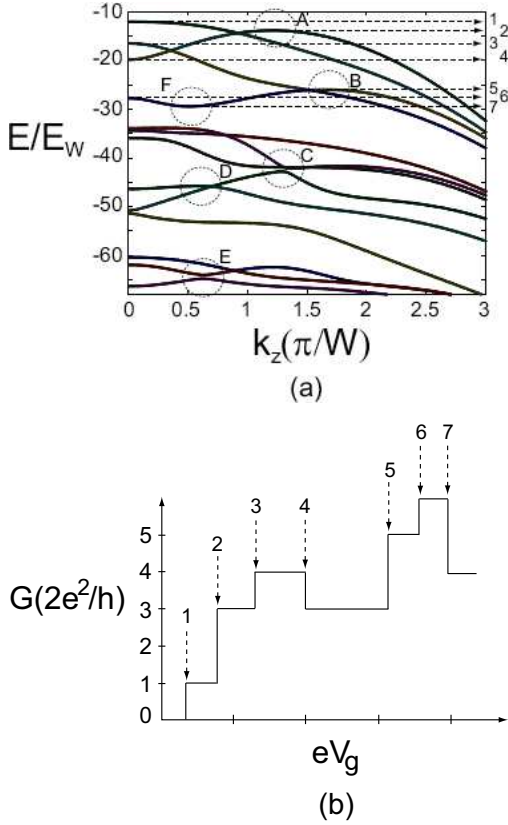


FIG. 11: (a) Zero-field hole-nanowire subband dispersions for a square cross-section hard-wall nanowire. The energy has been normalized by  $E_W = \gamma_1 \hbar^2 / (2m_0 W_x^2)$ . The hole nanowire states were obtained by numerical diagonalization of the cubic-symmetry Hamiltonian  $H_L + V_{\text{rh}}(x, y)$ . Dashed arrows indicate extremal values of subband dispersions that would be associated with steps in the two-terminal hole-wire conductance. (b) Schematic dependence on side-gate voltage for the linear two-terminal conductance through a hole nanowire or quantum point contact, based on the hole-subband dispersions shown in (a). Each conductance step corresponds to the Fermi energy reaching a value indicated by the dashed arrows.

top or side gate close to the nanowire or quantum point contact device. Application of a gate voltage essentially tunes the Fermi level (top gate) or the effective lateral confinement (side gate) of the nanowire or quantum point contact device such that different parts of the energy spectrum fall within the small energy window around the Fermi level in which conduction is possible. In conventional<sup>77,78</sup> zero-field quantized conductance spectra, the conductance changes monotonically in steps of  $2e^2/h$  as a function of gate voltage. This corresponds to the case of subband edges at  $k_z = 0$  entering the energy window which is allowed for transport around the Fermi level. A hole nanowire can display quite a different conductance spectrum due to its strong non-parabolic dispersion. For a hole nanowire with the dispersion shown in Fig. 11(a), the conductance can both *increase* and *decrease* in steps of  $2e^2/h$  and also  $2 \times (2e^2/h)$ . This behavior is caused by off-center subband maxima, examples of which are seen at points A and B in the hole dispersion shown in Fig. 11(a), as well as switches

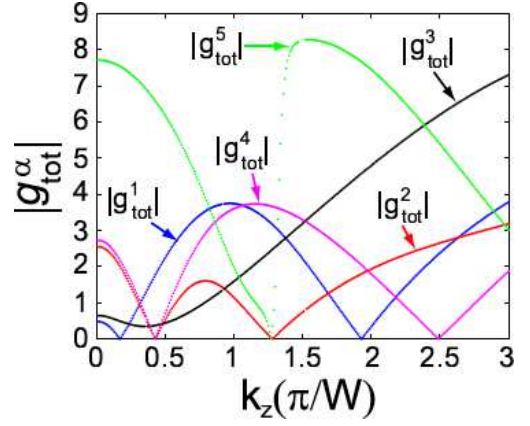


FIG. 12: (Color online) Absolute values of hole-wire  $g$  factors  $g_{\text{tot}}^\alpha$  for states at finite wave vector  $k_z$  for motion parallel to the wire axis. Results are shown for the subbands with  $\alpha = 1 \dots 5$ .

between hole-like and electron-like dispersion, as is the case for point F. A measurement of the transport properties in the linear-response regime can thus yield insight to the detailed structure of the hole nanowire subband dispersions.

In the presence of a magnetic field, the degeneracy of the hole nanowire subbands is lifted. Similar to the so far discussed spin splitting of the subband edges at  $k_z = 0$ , the spin splitting of the off-center maxima can also be probed by transport or optical measurements. For the square-cross-section wire with dispersion shown in Fig. 11(a), we have three off-center maxima; at points A, B, and D. Calculation of the spin splitting at these three points for a small magnetic field yields the  $g$  factor magnitudes  $g_{\text{tot}}^A = 2.25$ ,  $g_{\text{tot}}^B = 2.89$ , and  $g_{\text{tot}}^D = 4.20$ , respectively. The full dependence of the  $g$  factors of states in the five highest hole-wire subbands as a function of  $k_z$  is shown in Fig. 12. Interestingly, the  $g$  factor shows a strong dependence on  $k_z$ ; displaying an oscillatory variation and vanishing intermittently for most subbands.

## V. DISCUSSION AND CONCLUDING REMARKS

We have calculated Zeeman splitting of states in hole nanowires, subject to a magnetic field  $B_z$  pointing parallel to the wire axis (the  $z$  direction) and defined by three different types of confinement (cylindrical hard-wall, cylindrical soft-harmonic, and rectangular hard-wall). Our main focus has been to elucidate the properties of zone-center subband-edge states, although a few results are also given for hole-wire states having finite wavevector  $k_z$  for motion along the wire. We have disentangled spin-splitting contributions arising from (a) the bulk-hole Zeeman effect in the semiconductor material, and (b) the coupling of the applied magnetic field to the orbital wire bound states. We termed the contribution (a) the bulk-material contribution to the  $g$  factor and indicated it by the symbol  $g_z^\alpha$ , where the index  $\alpha$  labels the quasi-1D hole-wire subbands. The orbital contribution (b) turned out to have two separate terms. The one indicated by  $g_{\text{orb,diag}}^\alpha$  reflects the direct coupling of hole orbital angular momentum component

$\hat{L}_z$  with the magnetic field and displays HH-LH splitting, and the second one, labelled  $g_{\text{orb,mix}}^\alpha$ , arises from HH-LH mixing.

Quantum confinement of holes in a wire renders their eigenstates to be coherent superpositions of HH and LH components. Although these are pure states in the quantum-statistical sense, the spin polarization of such HH-LH mixed states is not fixed to be 3/2 as a simple analogy with spin-1/2 systems would suggest. We have used the recently discussed<sup>63</sup> invariant-multipole decomposition of the spin-3/2 density matrix to universally characterize spin polarization of hole-wire subband edge states. Within limits, the properties of low index (highest-in-energy) hole subbands turned out to be quite robust with respect to changes in wire cross-sectional shape and confinement strength. Also, many qualitative features are already captured within models where band-warping due to cubic crystal symmetry is neglected.

HH-LH mixing is illustrated by radial profiles of the spin-3/2 dipole moment (i.e., spin polarization) and turns out to have a profound impact on spin splitting. Variations in the spin-polarization profiles between different subband-edge states are reflected in fluctuations of the individual  $g$ -factor contributions, as well as the total nanowire-hole  $g$  factor. It is possible, by addressing different hole-subband edges, to study nontrivial hole spin-polarization states that have no counterpart in spin-1/2 systems, such as zero-polarizations states that have a large spin-3/2 octupole component. The bulk-material contribution to the hole-wire  $g$  factor could be investigated separately in wires made from diluted-magnetic semiconductor materials, where its magnitude can exceed that of the orbital terms by a few orders of magnitude.

The spin-splitting properties of individual hole-wire subband edges turn out to be tunable by changing the aspect ratio in a rectangular-cross-section wire geometry. This is of interest to applications involving electrostatically defined quantum point contacts or gated self-assembled wires, where the wire

shape can be manipulated *in situ*.

Our calculations were performed using Luttinger parameters for GaAs. However, results obtained within the spherical approximation will apply to other materials having a similar ratio  $\gamma_s/\gamma_1$ . The exact quantitative results will probably be different once cubic corrections are taken into account. However, as our comparison between fully cubic and approximate spherical models has shown, qualitative trends for low-index hole-wire subband edges are already captured in the spherical model. Hence, we believe that our results can be applied to materials other than GaAs.

The effects of linear-in-wavevector spin-orbit couplings has not been considered. The relative strength of bulk-inversion-asymmetry (BIA) induced  $\mathbf{k}$ -linear terms, as compared with leading-order terms in the Luttinger Hamiltonian, depends strongly on the material and the direction of motion with respect to crystallographic axes.<sup>39</sup> Given that cubic corrections have not been too important for low-lying hole-wire subband edges, we expect the same to hold for BIA terms. Also, while previous studies have shown that, in principle, electric fields applied perpendicular to nanowires affect hole  $g$  factors<sup>79</sup> (essentially because the HH-LH mixing changes), this effect becomes relevant only at quite large field magnitudes that are not likely to exist in typical point-contact or nanowire samples.

#### Acknowledgments

DC gratefully acknowledges support from the Massey University Research Fund and also thanks the Division of Solid State Physics/Nanometer Structure Consortium, Lund University, Sweden, for their hospitality and the Swedish Research Council (VR) for their financial support during the part of the work that was performed in Sweden.

- 
- <sup>1</sup> K. Hiruma, M. Yazawa, T. Katsuyama, K. Ogawa, K. Haraguchi, and H. Kakibayashi, *J. Appl. Phys.* **77**, 447 (1995).
  - <sup>2</sup> M. S. Gudiksen, J. Wang, and C. M. Lieber, *J. Phys. Chem. B* **105**, 4062 (2001).
  - <sup>3</sup> X. Duan, Y. Huang, Y. Cui, J. Wang, and C. M. Lieber, *Nature* **409**, 66, (2001).
  - <sup>4</sup> Z. Tang, N. A. Kotov, and M. Giersig, *Science* **297**, 237 (2002).
  - <sup>5</sup> D. Katz, T. Wizansky, O. Millo, E. Rothenberg, T. Mokari, and U. Banin, *Phys. Rev. Lett.* **89**, 086801 (2002); *ibid.* 199901 (2002)
  - <sup>6</sup> J. C. Johnson, H. J. Choi, K. P. Knutsen, R. D. Schaller, P. D. Yang, R. J. Saykally, *Nat. Mater.* **1**, 106 (2002).
  - <sup>7</sup> M. T. Björk, B. J. Ohlsson, T. Sass, A. I. Persson, C. Thelander, M. H. Magnusson, K. Deppert, L. R. Wallenberg, and L. Samuelson, *Nano Lett.* **2**, 87 (2002).
  - <sup>8</sup> M. T. Björk, B. J. Ohlsson, C. Thelander, A. I. Persson, K. Deppert, L. R. Wallenberg, and L. Samuelson, *Appl. Phys. Lett.* **81**, 4458 (2002).
  - <sup>9</sup> M. S. Gudiksen, L. J. Lauhon, J.-F. Wang, D. C. Smith, and C. M. Lieber, *Nature* **415**, 617 (2002).
  - <sup>10</sup> U. Krishnamachari, M. Borgström, B. J. Ohlsson, N. Panev, L. Samuelson, W. Seifert, M. W. Larsson and L. R. Wallenberg, *Appl. Phys. Lett.* **85**, 2077 (2004).
  - <sup>11</sup> L. Samuelson, M. T. Björk, K. Deppert, M. Larsson, B. J. Ohlsson, N. Panev, A. I. Persson, N. Sköld, C. Thelander and L. R. Wallenberg, *Physica E* **21**, 560 (2004)
  - <sup>12</sup> Y. Huang, X. Duan and C. M. Lieber, *Small* **1**, 142 (2005).
  - <sup>13</sup> C. Thelander, H. A. Nilsson, L. E. Jensen and L. Samuelson, *Nano Lett.* **5**, 635 (2005).
  - <sup>14</sup> C. Yang, Z. Zhong, C. M. Lieber, *Science* **310**, 1304 (2005).
  - <sup>15</sup> W. Lu, C. M. Lieber, *J. Phys. D* **39**, R387 (2006).
  - <sup>16</sup> P. Pauzauskie, P. Yang, *Materials Today* **9**, 36 (2006).
  - <sup>17</sup> A. I. Persson, M. T. Björk, S. Jeppesen, J. B. Wagner, L. R. Wallenberg and L. Samuelson, *Nano Lett.* **6**, 403 (2006).
  - <sup>18</sup> L. Samuelson, *Nanotechnology* **17**, (2006).
  - <sup>19</sup> J. Johansson, L. S. Karlsson, C. P. T. Svensson, T. Mårtensson, B. A. Wacaser, K. Deppert, L. Samuelson and W. Seifert, *Nat. Mater.* **5**, 574 (2006).
  - <sup>20</sup> E. Janik, J. Sadowski, P. Dłużewski, S. Kret, L. T. Baczewski, A. Petrouchik, E. Łusakowska, J. Wrobel, W. Zaleszczyk, G. Karczweski, and T. Wojtowicz, *Appl. Phys. Lett.* **89**, 133114 (2006).
  - <sup>21</sup> C. Thelander, P. Agarwal, S. Brongersma, J. Eymery, L. F. Feiner, A. Forchel, M. Scheffler, W. Riess, B. J. Ohlsson, U. Gösele and

- L. Samuelson, *Materials Today* **9**, 28 (2006).
- <sup>22</sup> F. Martelli, S. Rubini, M. Piccin, G. Bais, F. Jabeen, S. De Franceschi, V. Grillo, E. Carlino, F. D'Acapito, F. Boscherini, S. Cabrini, M. Lazzarino, L. Businaro, F. Romanato, and A. Franciosi, *Nano Lett.* **6**, 2130 (2006).
- <sup>23</sup> J. Xiang, W. Lu, Y. Hu, Y. Wu, H. Yan, and C. M. Lieber, *Nature* **441**, 489 (2006).
- <sup>24</sup> X. Feng, R. He, P. Yang, M. Roukes, *Nano Lett.* **7**, 1953 (2007).
- <sup>25</sup> S. Neretina, R. A. Hughes, J. F. Britten, N. V. Sochinskii, J. S. Preston, and P. Mascher, *Nanotechnology* **18**, 275301 (2007).
- <sup>26</sup> H.-Y. Li, O. Wunnicke, M. T. Borgström, W. G. G. Immink, M. H. M. van Weert, M. A. Verheijen, and E. P. A. M. Bakkers, *Nano Lett.* **7**, 1144 (2007).
- <sup>27</sup> Q. Zhu, K. F. Karlsson, E. Pelucchi, and E. Kapon, *Nano Lett.* **7**, 2227 (2007).
- <sup>28</sup> A. I. Hochbaum, R. Chen, R. D. Delgado, W. Liang, E. C. Garnett, M. Najarian, A. Majumdar, P. Yang, *Nature* **451**, 163 (2008).
- <sup>29</sup> B. S. Sørensen, M. Aagesen, C. B. Sørensen, P. E. Lindelof, K. L. Martinez, and J. Nygård, *Appl. Phys. Lett.* **92**, 012119 (2008).
- <sup>30</sup> M. S. Song, J. H. Jung, Y. Kim, Y. Wang, J. Zou, H. J. Joyee, Q. Gao, H. H. Tan, and C. Jagadish, *Nanotechnology* **19**, 125602 (2008).
- <sup>31</sup> S. Roddaro, A. Fuhrer, P. Brusheim, C. Fasth, H. Q. Xu, L. Samuelson, J. Xiang, and C. M. Lieber, *Phys. Rev. Lett.* **101**, 186802 (2008).
- <sup>32</sup> W. Zaleszczyk, E. Janik, A. Presz, P. Dłużewski, S. Kret, W. Szuszkiewicz, J.-F. Morhange, E. Dynowska, H. Kirmse, W. Neumann, A. Petrouchik, L. T. Baczewski, G. Karczewski, and T. Wojtowicz, *Nano Lett.* **8**, 4061 (2008).
- <sup>33</sup> S. A. Wolf, D. D. Awschalom, R. A. Buhrmann, J. M. Daughton, S. von Molnár, M. L. Roukes, A. Y. Chtchelkanova, and D. M. Treger, *Science* **294**, 1488 (2001).
- <sup>34</sup> I. Zutic, J. Fabian, and S. Das Sarma, *Rev. Mod. Phys.* **76**, 323 (2004).
- <sup>35</sup> R. Fiederling, M. Keim, G. Reuscher, W. Ossau, G. Schmidt, A. Waag, and L. W. Molenkamp, *Nature* **402**, 787 (1999).
- <sup>36</sup> Y. Ohno, D. K. Young, B. Beschoten, F. Matsukura, H. Ohno, and D. D. Awschalom, *Nature* **402**, 790 (1999).
- <sup>37</sup> Y. A. Bychkov and E. I. Rashba, *J. Phys. C* **17**, 6039 (1984).
- <sup>38</sup> S. Datta and B. Das, *Appl. Phys. Lett.* **56**, 665 (1990).
- <sup>39</sup> R. Winkler, *Spin-Orbit Coupling Effects in Two-Dimensional Electron and Hole Systems* (Springer, Berlin, 2003).
- <sup>40</sup> R. Winkler, S. J. Papadakis, E. P. De Poortere, and M. Shayegan, *Phys. Rev. Lett.* **85**, 4574 (2000).
- <sup>41</sup> R. Danneau, O. Klochan, W. R. Clarke, L. H. Ho, A. P. Micolich, A. R. Hamilton, M. Y. Simmons, M. Pepper, D. Ritchie, and U. Zülicke, *Phys. Rev. Lett.* **97**, 026403 (2006).
- <sup>42</sup> S. P. Koduyavur, L. P. Rokhinson, D. C. Tsui, L. N. Pfeiffer, and K. W. West, *Phys. Rev. Lett.* **100**, 126401 (2008).
- <sup>43</sup> S. J. Prado, C. Trallero-Giner, A. M. Alcalde, V. López-Richard, and G. E. Marques, *Phys. Rev. B* **69**, 201310 (2004).
- <sup>44</sup> C. E. Pryor, and M. E. Flatté, *Phys. Rev. Lett.* **96**, 026804 (2006).
- <sup>45</sup> X.-W. Zhang, W.-J. Fan, K. Chang, S.-S. Liu, and J.-B. Xia, *Appl. Phys. Lett.* **91**, 113108 (2007).
- <sup>46</sup> K.-M. Haendel, R. Winkler, U. Denker, O. G. Schmidh, and R. J. Haug, *Phys. Rev. Lett.* **96**, 086403 (2006).
- <sup>47</sup> J. M. Luttinger, *Phys. Rev.* **102**, 1030 (1956).
- <sup>48</sup> K. Suzuki and J. C. Hensel, *Phys. Rev. B* **9**, 4184 (1974).
- <sup>49</sup> E. I. Rashba and E. Yu. Sherman, *Phys. Lett. A* **129**, 175 (1988).
- <sup>50</sup> C. Lü, J. L. Cheng, and M. W. Wu, *Phys. Rev. B* **73**, 125314 (2006).
- <sup>51</sup> G. Bastard, J. A. Brum, and R. Ferreira, *Solid State Physics* (Academic Press, San Diego, 1991), vol. 44, pp. 229-415.
- <sup>52</sup> M. P. Persson and H. Q. Xu, *Nano Lett.* **4**, 2409 (2004); *Phys. Rev. B* **73**, 125346 (2006).
- <sup>53</sup> X. W. Zhang, Y. H. Zhu, and J. B. Xia, *Eur. Phys. J. B* **52**, 133 (2006).
- <sup>54</sup> Y. Harada, T. Kita and O. Wada, *Phys. Rev. B* **74**, 245323 (2006).
- <sup>55</sup> D. Csontos and U. Zülicke, *Phys. Rev. B* **76**, 073313 (2007).
- <sup>56</sup> F. V. Kyrchenko, and J. Kossut, *Phys. Rev. B* **70**, 205317 (2004).
- <sup>57</sup> L. C. Lew Yan Voon, R. Melnik, B. Lassen, M. Willatzen, *Nano Lett.* **4**, 289 (2004).
- <sup>58</sup> W. Sheng, and A. Babinski, *Phys. Rev. B* **75**, 033316 (2007).
- <sup>59</sup> V. Troncale, K. F. Karlsson, E. Pelucchi, A. Rudra, and E. Kapon, *Appl. Phys. Lett.* **91**, 241909 (2007).
- <sup>60</sup> D. Csontos and U. Zülicke, *Appl. Phys. Lett.* **92**, 023108 (2008).
- <sup>61</sup> D. Csontos, U. Zülicke, P. Brusheim, and H. Q. Xu, *Phys. Rev. B* **78**, 03307 (2008).
- <sup>62</sup> P. Chen, *Phys. Rev. B* **72**, 045335 (2005).
- <sup>63</sup> R. Winkler, *Phys. Rev. B* **70**, 125301 (2004).
- <sup>64</sup> H. T. Ng, J. Han, T. Yamada, P. Nguyen, Y. P. Chen, M. Meyyappan, *Nano Lett.* **4**, 1247 (2004).
- <sup>65</sup> T. Bryllert, L. E. Wernersson, L. E. Froberg, L. Samuelson, *IEEE Electron Dev. Lett.* **27**, 323 (2006).
- <sup>66</sup> Q. Wang, N. Carlsson, I. Maximov, P. Omling, L. Samuelson, W. Seifert, W. Sheng, I. Shorubalko, and H. Q. Xu, *Appl. Phys. Lett.* **76**, 2274 (2000).
- <sup>67</sup> R. Danneau, W. R. Clarke, O. Klochan, A. P. Micolich, A. R. Hamilton, M. Y. Simmons, M. Pepper, and D. A. Ritchie, *Appl. Phys. Lett.* **88**, 012107 (2006).
- <sup>68</sup> O. Klochan, W. R. Clarke, R. Danneau, A. P. Micolich, L. H. Ho, A. R. Hamilton, K. Muraki, and Y. Hirayama, *Appl. Phys. Lett.* **89**, 092105 (2006).
- <sup>69</sup> B. Grbić, R. Leturcq, T. Ihn, K. Ensslin, D. Reuter, and A. D. Wieck, *AIP Conf. Proc.* **893**, 777 (2007).
- <sup>70</sup> A. Baldereschi and N. O. Lipari, *Phys. Rev. B* **8**, 2697 (1973).
- <sup>71</sup> A. Baldereschi and N. O. Lipari, *Phys. Rev. B* **9**, 1525 (1974).
- <sup>72</sup> P. C. Sercel and K. J. Vahala, *Appl. Phys. Lett.* **57**, 545 (1990).
- <sup>73</sup> P. C. Sercel and K. J. Vahala, *Phys. Rev. B* **42**, 3690 (1990).
- <sup>74</sup> I. Vurgaftman, J. R. Meyer, and L. R. Ram-Mohan, *J. Appl. Phys.* **89**, 5815 (2001).
- <sup>75</sup> M. P. Persson and H. Q. Xu, *Appl. Phys. Lett.* **81**, 1309 (2002).
- <sup>76</sup> T. Dietl, H. Ohno, and F. Matsukura, *Phys. Rev. B* **63**, 195205 (2001).
- <sup>77</sup> B. J. van Wees, H. van Houten, C. W. J. Beenaker, J. G. Williamson, L. P. Kouwenhoven, D. van der Marel, and C. T. Foxon, *Phys. Rev. Lett.* **60**, 848 (1988).
- <sup>78</sup> D. A. Wharam, T. J. Thornton, R. Newbury, M. Pepper, H. Ahmed, J. E. F. Frost, D. G. Hasko, D. C. Peacock, D. A. Ritchie, and G. A. C. Jones, *J. Phys. C* **21**, L209 (1988).
- <sup>79</sup> X. W. Zhang and J. B. Xia, *J. Phys. D* **40**, 541 (2007).